Title: Estimation of micro-Hall-Petch coefficients for prismatic slip system in Mg-4Al as a function of grain boundary parameters

Authors: Mohsen Taheri Andani[a*,b], Aaditya Lakshmanan[c], Veera Sundararaghavan[c], John Allison[b], Amit Misra[a,b]

[a] Department of Mechanical Engineering, University of Michigan, Ann Arbor, MI, 48105, USA

[b] Department of Materials Science and Engineering, University of Michigan, Ann Arbor, MI, 48105, USA

[c] Department of Aerospace Engineering, University of Michigan, Ann Arbor, MI, 48105, USA

*Communicating Author contact information: Mohsen Taheri Andani
Mailing address: 3062 H dH Dow Bldg, 2300 Hayward Street, Ann Arbor, Michigan, 48109
Email address: mtaheri@umich.edu
Phone number: 734-763-2445
Fax number: 734-763-4788

Other authors:

Aaditya Lakshmanan (aadityal@umich.edu)

Veera Sundararaghavan (veeras@umich.edu)

John Allison (johnea@umich.edu)

Amit Misra (amitmis@umich.edu)

Abstract

Grain size strengthening, referred to as the Hall-Petch effect, is a common strategy to improve the yield strength of magnesium (Mg) alloys. Several experimental studies have reported that the Hall-Petch slope strongly depends on the texture of the alloy. This effect arises from altering grain boundaries (GBs) resistance to different slip systems to transfer across adjacent grains. The grain boundary barrier strength of certain grain boundaries to basal slip, referred to as basal micro-Hall-Petch, was investigated in the previous work. In this study, the micro-Hall-Petch coefficient values for the prismatic slip ($k_\mu^{prismatic}$) in Mg-4Al and their correlation with the grain boundary parameters were investigated. An experimental method was developed to initiate the prismatic slip band at low-stress levels. High-resolution electron backscatter diffraction (HR-EBSD) was used to measure the residual stress tensor, from which the resolved shear stress ahead of blocked prismatic slip bands was computed for seven different grain boundaries. $k_\mu^{prismatic}$ values for each individual GB were calculated by coupling the stress profile information with a continuum dislocation pile-up model. The $k_\mu^{prismatic}$ values vary from 0.138 $MPa.m^{1/2}$ to 0.685 $MPa.m^{1/2}$ which are almost three times larger than the calculated values for the basal micro-Hall-Petch. The $k_\mu^{prismatic}$ values were correlated with the GB parameters, and a functional relationship depending on the two most effective angles, the angle between the traces of the slip planes on the GB plane (θ) and the angle between incoming and outgoing slip directions (κ), was proposed to estimate the Hall-Petch barrier for prismatic slip system. The work provides coefficients that can be supplied as input to crystal plasticity models to couple the effect of texture and grain size effectively.

1 Introduction

Owing to their low mass density, Mg alloys are attractive candidates for a range of industrial applications such as automotive [1], aerospace [2], and biomedical [3, 4] sections. However, the wide use of Mg alloys is limited by the low yield strength and formability at room temperature compared to the other structural materials such as aluminum and titanium. Alternative strategies to engineer the microstructure of Mg alloys to improve the yield strength and strain hardening include grain size refinement [5, 6], precipitate strengthening [7-10], solute strengthening [11-13], and texture modifications [14, 15].

Grain size strengthening is one of the most common strategies to enhance the yield strength of Mg alloys. The empirical Hall-Petch relationship defines the yield strength (σ_y) of a material as a function of its average grain size (D) following $\sigma_y = \sigma_0 + \frac{K}{\sqrt{D}}$, where K is the Hall-Petch coefficient and σ_0 is the friction stress [16-19]. Several experimental studies investigated the Hall-Petch relationship in Mg alloy and indicate that the Hall-Petch coefficient strongly depends on the texture of the alloy [5, 20-22]. For example, Yuan $et\ al.$ [5] reported that the Hall-Petch coefficient for Mg–3Al–1Zn varies from 0.411 MPa. $m^{1/2}$ to 0.228 MPa. $m^{1/2}$ by changing the loading direction along two orthogonal directions. The reported correlation between the Hall-Petch slope and texture in Mg alloys is primarily due to the underlying crystal structure, hexagonal close-packed (HCP), being plastically anisotropic, i.e., the presence of different deformation modes with unequal strengths in these alloys. Texture variations can lead to activation of different deformation modes/systems, on which the GBs resistance to them can have a different effect, which results in altering the Hall-Petch coefficient.

To better understand the interactions of the Hall-Petch effect (grain size), texture, and grain boundary parameters, in the strengthening of materials, the Hall-Petch relationship needs to be investigated at the slip system level for each individual deformation mode. The Hall-Petch relationship extended to the microscale is given by $\tau^\alpha = \tau_0^\alpha + k_\mu^\alpha . L^{\alpha - 1/2}$, where τ^α is the critical resolved shear stress corresponding to slip system α, τ_0^α is the critical resolved shear stress corresponding to slip system α of a theoretically infinite single crystal, k_μ^α the microscopic Hall-Petch coefficient of the slip system α (micro-Hall-Petch coefficient), and L^α is the grain size at the slip system-level for system α [23-25]. Since experimental approaches to quantify the stress tensor at the grain level are limited, very few studies focused on finding the micro-Hall-Petch coefficients for each individual slip system and the subsequent effect on the macroscopic Hall-Petch relationship [20, 26, 27]. Wang *et al.* [20] used the macroscopic tensile data of Mg–3Al–1Zn samples and estimate the variation of the resolved shear stress for each individual slip system by changing the grain size to calculate the micro-Hall-Petch slopes. They reported the micro-Hall-Petch coefficients for basal slip, prismatic slip, and pyramidal slip to be $0.091 \text{MPa}. \text{m}^{1/2}$, $0.154 \text{ MPa}. \text{m}^{1/2}$ and $0.311 \text{ MPa}. \text{m}^{1/2}$, respectively. In our previous works [28, 29], we proposed using HR-EBSD to measure the local stress at the grain level and calculate the micro-Hall-Petch coefficient values for the basal slip in Mg alloys. The results show the micro-Hall-Petch coefficient values for the basal slip in Mg-4Al varies from $0.054 \text{ MPa}. \text{m}^{1/2}$ to $0.184 \text{ MPa}. \text{m}^{1/2}$ depending on the angle between incoming slip direction and the potential outgoing slip direction, and the angle between the two slip plane intersections with the GB.

In this paper, we further expand on our previous results in order to understand the micro-Hall-Petch relationship for prismatic slip system in Mg-4Al. First, we present a novel method using micro-focused ion beam (FIB) notches to locally activate prismatic slip bands. We then use

HR-EBSD measurements to assess the stress ahead of prismatic slip bands blocked at seven different GBs. The results are compared with a developed continuum dislocation pile-up model considering the presence of micro-FIB notch under two different boundary conditions to calculate the micro-Hall-Petch coefficient for prismatic slip systems. FIB milling is used to capture the three-dimensional grain boundary parameters (tilt and twist angles) of each individual grain boundary. A functional form to find the micro-Hall-Petch coefficient values of prismatic slip depending on the grain boundary descriptors is proposed, and the potential way to implement it to crystal plasticity constitutive models is discussed.

2   Methods

2.1   Materials and experimental procedures

Mg-4Al (wt.%) produced by CanmetMaterials in the form of extruded bar is used in this study. The texture of the as-extruded material is shown in Figure 1a. The basal poles are oriented normal to the extrusion direction. This texture leads to activation of primarily basal and prismatic slip systems during plasticity when the loading direction is parallel to the extrusion direction. The average grain size of the as-received material was 55 µm. Further heat treatment is conducted to produce samples with average grain sizes of approximately 187 µm (515°C for 15 minutes) and 333 µm (550°C for 150 minutes) with a texture very similar to that shown in Figure 1a. Tensile tests are performed at a strain rate of $1 \times 10^{-3} \ s^{-1}$ for the samples with different grain sizes up to 2% strain. Figure 1b depicts the variation of the yield strength (0.2% offset) with average grain size, reflecting the Hall-Petch effect for this alloy. The linear fit of this data results in a Hall-Petch slope of 0.372 $\mathrm{MPa.\,m^{1/2}}$, consistent with previous findings for Mg-4Al [30].
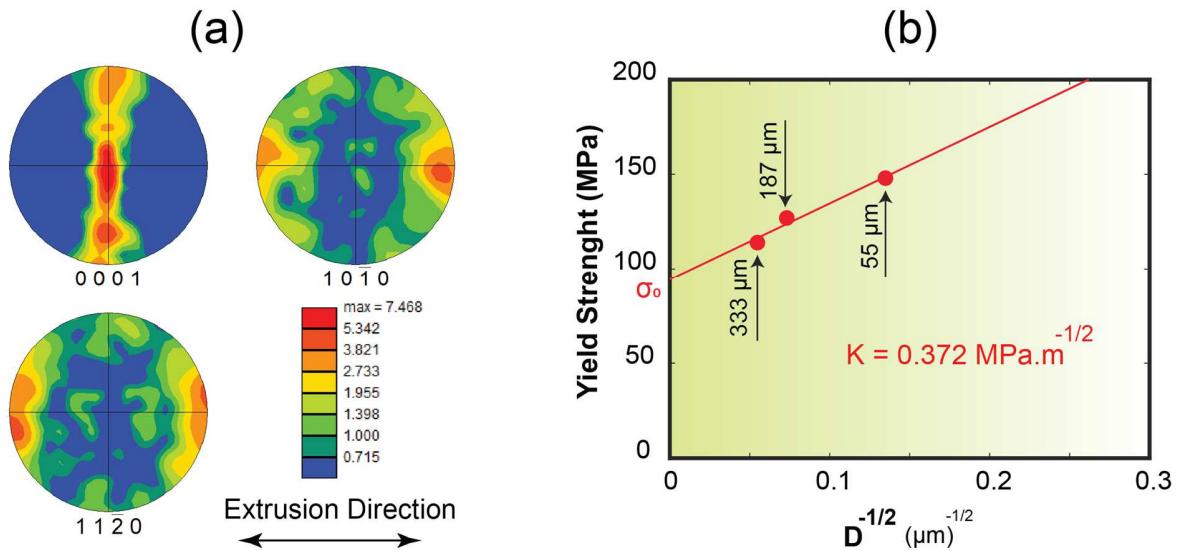
Figure 1: (a) Pole figure and (b) Hall-Petch relationship of extruded Mg-4Al (wt.%) sample used in this work. Linear fit yields $\sigma_0 = 94.33\ MPa$, $K = 0.372\ \text{MPa.m}^{1/2}$.

Figure 2 depicts a microstructure section of the sample with the average grain size of 55 µm, which is primarily composed of equiaxed grains. From this sample, specimens with the gauge dimensions of 10 mm × 2 mm × 2 mm are cut using electrical discharge machining (EDM). The samples are then mechanically ground using SiC papers up to a grit of 1200. Polishing is completed using 6, 3, and 1 µm diamond suspensions, followed by a final polish using Buehler Masterpolish on a Buehler Chemomet polishing cloth. Samples are lightly chemically etched in acetic-nitric solution (60 mL ethanol, 20 mL water, 15mL acetic acid, and 5 mL nitric acid) for 3-5 seconds to highlight the grain boundaries.

Figure 2: EBSD inverse pole figure map of extruded Mg-4Al (wt.%) with the average grain size of 55 µm.

Our primary goal in this study is to initiate prismatic slip in the form of localized slip bands which would then be blocked by the grain boundary. It is well known that the anisotropy of the HCP crystal structure reflects significantly higher critical resolved shear stress for prismatic relative to the basal slip system. To preferentially activate prismatic slip at the low level of stress (which is important to consider for capturing high-resolution Kikuchi patterns) a series of sharp micro-notches are machined in grains oriented (relative to the loading direction) specifically for the prismatic slip to act as slip initiation sites. Given the EBSD data of the microstructure section (Figure 2), grains were chosen which satisfied the following conditions:

1. There is at least one prismatic slip system with a Schmid factor (corresponding to tension along the extrusion direction) greater than or equal to 0.4. This was to ensure that there is at least one prismatic slip system-oriented favorably for plastic slip relative to loading.

2. The ratio of the maximum Schmid factor of basal to the maximum Schmid factor of prismatic is at most 0.2. This was to ensure that the basal system is not as favorably oriented as the prismatic system obtained from step 1.

3. For ease of fabricating the notch using FIB-milling, with prismatic systems obtained from step 1 having a plane normal lying favorably in the plane of the sample surface.

The above steps were automated using a MATLAB script which employed the MTEX toolbox [31, 32] to post-process EBSD data. Once the grains of interest are identified, the micro-notches were created using an FEI Helios Nanolab 650 microscope equipped with a gallium ion source (see Figure 3a). Notches are machined parallel to the prismatic slip plane, and each had an approximate length of 20 µm, a width of 1 µm, and a depth of 10 µm (Figure 3(b)). The orientation of the prismatic slip system is known due to orientation data available from EBSD.

The tensile samples are then subjected to loading to observe slip band generation from notches. Figure 3(c) shows two examples of slip bands that initiate from notches; one was blocked at the grain boundary (GB#1), and the other one transferred to the adjacent grain (GB#2). Seven-grain boundaries are analyzed for this work since our focus is on boundaries that blocked slip transfer. Table 1 summarizes the information of these GBs based on the misorientation between adjacent grains.

Kikuchi patterns ahead of blocked slip bands are captured using a TESCAN RISE microscope equipped with a Hikari Super EBSD detector provided by EDAX. The EBSD maps had an average size of 20 µm × 20 µm with a square grid, and 200 nm step size. The CrossCourt4 (CC4) software package developed by BLG Vantage is used to analyze the Kikuchi patterns and assess the full strain/stress fields across the grains by implementing the cross-

correlation approach developed by Wilkinson *et al*. [33]. The remapping method developed by Britton and Wilkinson [34] is also applied to minimize the effect of the lattice rotation on calculated strain/stress values.

Upon completing the EBSD analysis, the subsurface grain boundary orientations are measured to understand the grain boundary plane orientations. To accomplish this, FIB milling is used to lift out lamellae perpendicular to the grain boundary line using an FEI Helios Nanolab 650 microscope.
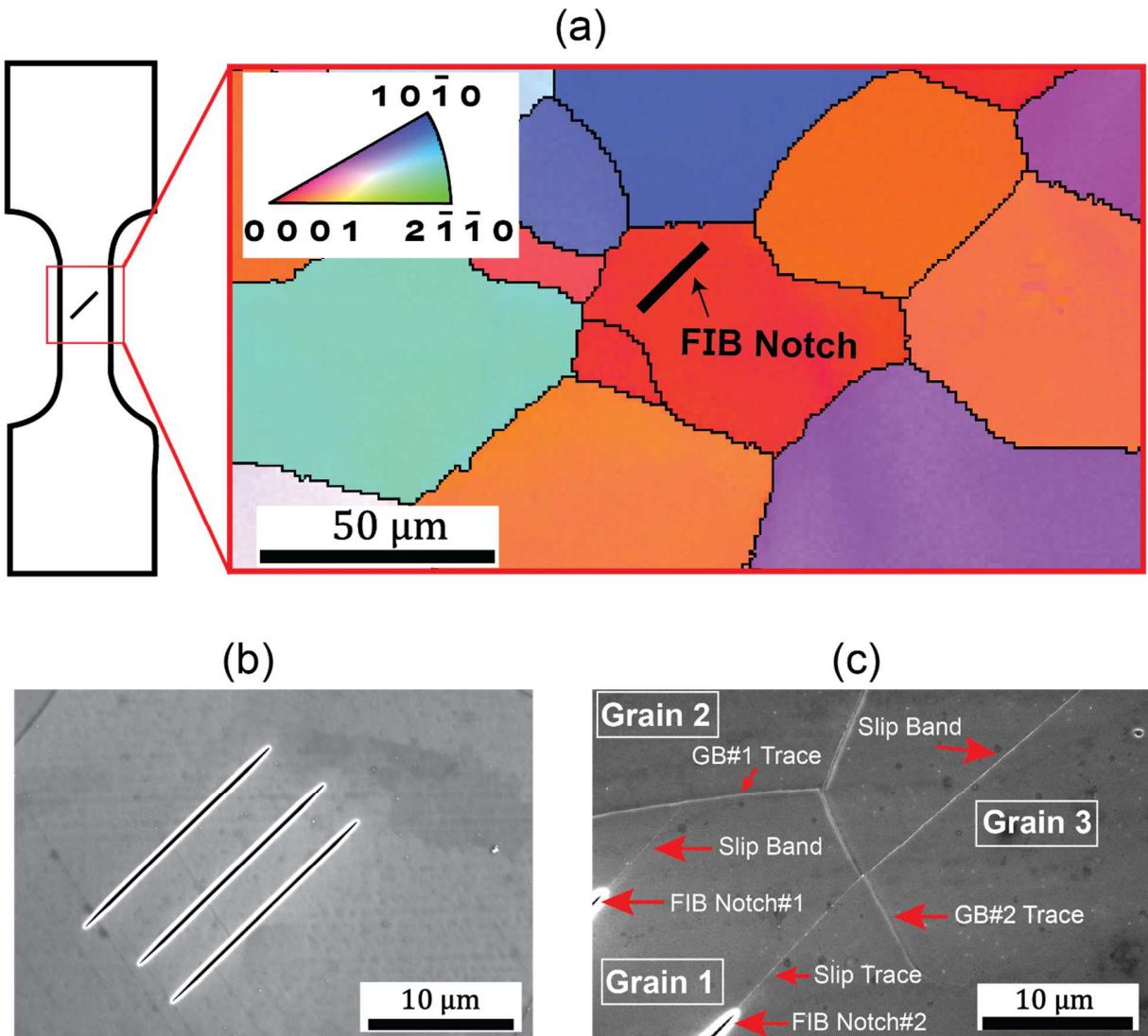
Figure 3: (a) Diagram showing placement of FIB notch parallel to prismatic slip planes, (b) Examples of micro-notch machined on the surface of the samples to act as slip initiation sites, (c) Example of slip bands initiate from FIB notch and interact with GBs. Slip transmission occurs in GB#2, and pile-up occurs in GB#1.

Table 1: Misorientation angle and rotation axis of the GBs investigated in this work.

GB Number	Misorientation (°)	Rotation Axis
1	84.70	$[\bar{6}\ 11\ \bar{5}\ 1]$
2	52.38	$[8\ \bar{9}\ 1\ 1]$
3	79.89	$[\overline{11}\ \bar{9}\ 20\ 1]$
4	62.67	$[9\ 3\ \overline{12}\ \bar{1}]$
5	65.61	$[\overline{17}\ \bar{2}\ 19\ 1]$
6	38.36	$[5\ 8\ \overline{13}\ 1]$
7	36.84	$[9\ 8\ \overline{17}\ 0]$

2.2 Analytical and Numerical Methods

This section is devoted to outlining the analytical and numerical methods that form the basis of our work. First, the continuum dislocation pile-up theory in 1D is reviewed, which furnishes a closed-form expression for the stress ahead of the pile-up. Following that, essential aspects of the rate-dependent crystal plasticity are described which are implemented into the PRISMS-Plasticity [35] crystal plasticity finite element(CPFE) framework. Finally, the calibration procedure to obtain constitutive model parameters is outlined, followed by the methodology to simulate neighborhoods of grain boundaries of interest-based on experimental data.

2.2.1 Dislocation Pile-up Model of Notch and Slip Band

A simple one-dimensional continuum dislocation pile-up model is used as an analogy to describe the region in the grain constituting the notch and the slip band (Figure 4). Both the notch and the slip band are represented by a continuous distribution of straight parallel edge dislocations [36,

37] with the dislocation line pointing in the z-direction, and Burgers vector along the $x-$direction with magnitude b_e.
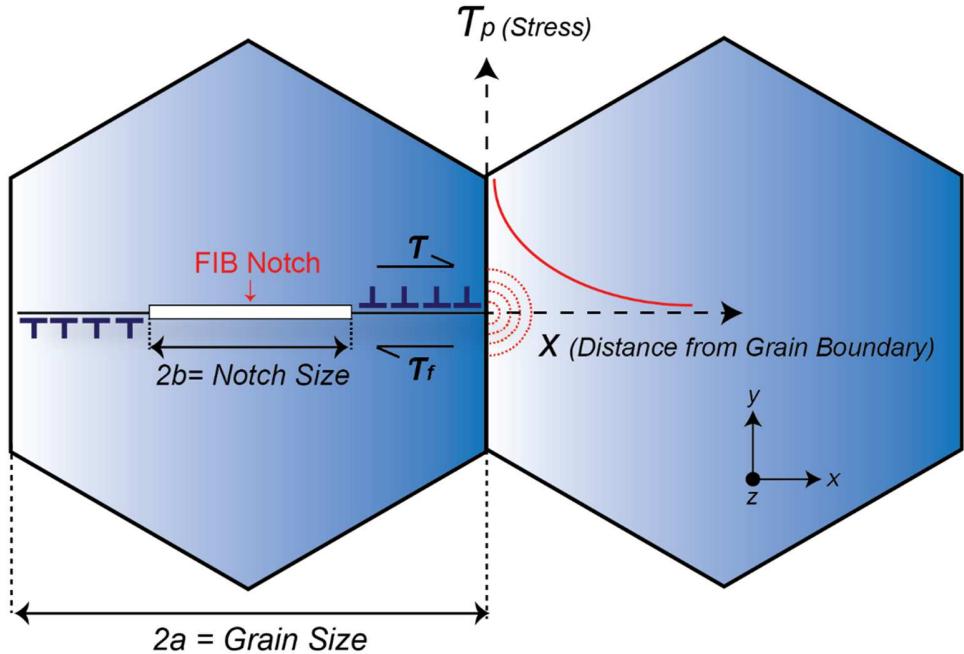

Figure 4: Notch and slip band idealized as a continuous distribution of parallel edge dislocations.

Let $\rho(x)$ denote the distribution of dislocations in the domain $[-a,a]$ where the subdomain $[-b,b]$ represents the notch. We would then like to solve for $\rho(x)$ which is in equilibrium with an effective resolved stress $\tau_e(x)$, where the equilibrium condition takes the following form [38]

$$\frac{\mu b_e}{2\pi(1-v)}\left\{\int_{-a}^{-b}\frac{\rho(x')dx'}{x-x'}+\int_{-b}^{b}\frac{\rho(x')dx'}{x-x'}+\int_{b}^{a}\frac{\rho(x')dx'}{x-x'}\right\}+\tau_e(x)=0$$

$$\tau_e(x)=\begin{cases}\tau & ;\ |x|<b\\\tau-\tau_f & ;\ b<|x|<a\end{cases}$$

(1)

where μ is the shear modulus, v is the Poisson's ratio and τ_f is a friction stress acting only in the slip band, which inhibits the motion of the prismatic dislocations. τ_f is assumed to be a constant.

We are interested in a closed-form expression for the resolved stress ahead of the pile-up, $\tau_p(x)$, defined as follows:

$$\tau_p(x) := \frac{\mu b_e}{2\pi(1-v)}\left\{\int_{-a}^{-b}\frac{\rho(x')dx'}{x-x'} + \int_{-b}^{b}\frac{\rho(x')dx'}{x-x'} + \int_{b}^{a}\frac{\rho(x')dx'}{x-x'}\right\} ; \; x > a \qquad (2)$$

Eqn. 1 is an integral equation with a closed-form solution [39] for $\rho(x)$, which upon substituting in Eqn. 2 yields

$$\tau_p(x) = \frac{\left(\tau - 2\tau_f\cos^{-1}\left(\frac{b}{a}\right)\right)}{\sqrt{1-\left(\frac{a}{x}\right)^2}} + 2\tau_f\csc^{-1}\left(\sqrt{1+\frac{(x^2-a^2)b^2}{(a^2-b^2)x^2}}\right) - \tau; \; x \\ > a \qquad (3)$$

Shifting the origin to $x = a$ by defining $X = x - a$, and substituting x in terms of X yields

$$\tau_p(X) = \frac{\left(\tau - 2\tau_f\cos^{-1}\left(\frac{b}{a}\right)\right)}{\sqrt{1-\left(\frac{a}{X+a}\right)^2}} + 2\tau_f\csc^{-1}\left(\sqrt{1+\frac{((X+a)^2-a^2)b^2}{(a^2-b^2)(X+a)^2}}\right) - \tau \qquad (4)$$

Eqn. (4) is now valid for $X > 0$. We now invoke the micro-Hall-Petch assumption [28, 29] where τ is additively decomposed into size-independent and size-dependent contributions. Since we invoke this at the level of the slip system, we replace τ with τ^α corresponding to slip system α. The decomposition then takes the simple form

$$\tau^\alpha = \tau_0^\alpha + \frac{k_\mu^\alpha}{\sqrt{2a}} \qquad (5)$$

where τ_0^α is the lattice friction stress for slip system α, k_μ^α is the micro-Hall-Petch coefficient and a is the grain size as defined in Figure 4. Substituting Eqn. 5 into Eqn. 4 and specializing to slip system α yields.

$$\tau_p^\alpha(X) = \frac{\left(\tau_0^\alpha + \frac{k_\mu^\alpha}{\sqrt{a-b}} - 2\tau_f^\alpha \cos^{-1}\left(\frac{b}{a}\right)\right)}{\sqrt{1-\left(\frac{a}{X+a}\right)^2}} + 2\tau_f^\alpha \csc^{-1}\left(\sqrt{1 + \frac{((X+a)^2 - a^2)b^2}{(a^2-b^2)(X+a)^2}}\right) - \tag{6}$$

$$\left(\tau_0^\alpha + \frac{k_\mu^\alpha}{\sqrt{2a}}\right)$$

Eqn. 6 furnishes an expression for the resolved stress ahead of the pile-up, which is fit to the data obtained from HR-EBSD residual stress measurements. Here a and b are known parameters since they are lengths which can be measured from the images (Figure 3). An estimate of τ_0^α is obtained using σ_0 (y-intercept in Figure 1(b)) and the average Schmid factor associated with prismatic slip for the present as-extruded texture. The average Schmid factor for prismatic slip is obtained by first computing the maximum Schmid factor for each orientation among the prismatic slip systems, and then finding the mean of those values. In our case, this value is 0.451, very similar to previous work[40] which reported a value of 0.43. σ_0 denotes the yield strength for the microstructure with theoretically infinite grain size, and multiplying this by the average Schmid factor for prismatic slip results in an estimate of the grain-size independent critical resolved shear stress for prismatic slip. In our case setting $\sigma_0 = 94.33\ MPa$ and using 0.451 as the Schmid factor for prismatic slip [40], yields $\tau_0^\alpha = 42.54\ MPa$. The parameters k_μ^α and τ_f^α are the unknowns which are optimized for by performing a least-squares fit of Eqn. 6 to the residual stress measurements.

2.2.2 Single Crystal Constitutive Model

We adopt a rate-dependent crystal plasticity constitutive model within the finite deformation continuum mechanics framework. The primary kinematic ingredient is the deformation gradient, $\mathbf{F}$, which maps infinitesimal material fibers in the reference configuration to corresponding fibers in the deformed configuration. We assume $\mathbf{F}$ to abide by a multiplicative decomposition [41, 42] into elastic and plastic components, denoted by $\mathbf{F}^e$ and $\mathbf{F}^p$, respectively, as follows:

$$\mathbf{F} = \mathbf{F}^e\mathbf{F}^p \tag{7}$$

Physically, $\mathbf{F}^p$ encodes the homogenized distortion of the body as a consequence of crystallographic slip via dislocation motion on specific slip systems. It maps the reference configuration to an intermediate configuration where the underlying lattice remains unchanged. $\mathbf{F}^e$, on the other hand, captures the elastic stretch and lattice rotation and maps the intermediate configuration to the deformed configuration. Since plasticity is inherently deformation path-dependent, we invoke certain deformation rates.

Using Eqn. (7), the velocity gradient, $\mathbf{L} = \dot{\mathbf{F}}\mathbf{F}^{-1}$, can then be expanded additively decomposed into elastic and plastic components

$$\mathbf{L} = \underbrace{\dot{\mathbf{F}}^e\mathbf{F}^{e-1}}_{\text{Elastic part}} + \underbrace{\mathbf{F}^e\dot{\mathbf{F}}^p\mathbf{F}^{p-1}\mathbf{F}^{e-1}}_{\text{Plastic part}} \tag{8}$$

The contributions to the velocity gradient from elastic and plastic parts are both defined in the deformed configuration. We can alternatively work with the plastic part of the velocity gradient defined on the intermediate configuration, $\mathbf{L}^p$, as:

$$\mathbf{L}^p = \dot{\mathbf{F}}^p\mathbf{F}^{p-1} \tag{9}$$

Noting that the kinematics of crystallographic slip effectively involves shearing of the lattice on specific crystallographic slip planes along with specific crystallographic slip directions, we have

$$\mathbf{L}^{\mathrm{p}} = \dot{\mathbf{F}}^{\mathrm{p}}\mathbf{F}^{\mathrm{p}-1} = \sum_{\alpha=1}^{n_s} \dot{\gamma}^{\alpha}\mathbf{m}^{\alpha}\otimes\mathbf{n}^{\alpha} = \sum_{\alpha=1}^{n_s} \dot{\gamma}^{\alpha}\mathbf{S}^{\alpha} \tag{10}$$

where $\dot{\gamma}^{\alpha}$ is the shearing rate on slip system α, n_s is the number of slip systems, $\mathbf{m}^{\alpha}$ and $\mathbf{n}^{\alpha}$ are slip direction and slip plane normal unit vectors, respectively. $\mathbf{S}^{\alpha}$, referred to as the Schmid tensor for the slip system α, is a shorthand for the dyadic product of $\mathbf{m}^{\alpha}$ and $\mathbf{n}^{\alpha}$. We note that $\mathbf{m}^{\alpha}$ and $\mathbf{n}^{\alpha}$ are crystallographic vectors in the intermediate configuration.

We adopt a rate-dependent crystal plasticity framework, where the shearing rate $\dot{\gamma}^{\alpha}$ is a function of the resolved shear stress τ^{α} through a phenomenological power law [43] as follows:

$$\dot{\gamma}^{\alpha} = \dot{\gamma}_0 \left|\frac{\tau^{\alpha}}{s^{\alpha}}\right|^{m} \mathrm{sign}(\tau^{\alpha}) \tag{11}$$

where $\dot{\gamma}_0$ is the reference shearing rate, m is the strain rate, sensitivity exponent, τ^{α} is the resolved shear stress on slip system α, s^{α} is the slip resistance on slip system α and 'sign' refers to the signum function. The resolved shear stress is expressed in terms of the second Piola-Kirchoff stress in the intermediate configuration [44, 45], $\mathbf{T}$, via the following relation

$$\tau^{\alpha} = (\mathbf{F}^{\mathrm{eT}}\mathbf{F}^{\mathrm{e}}\mathbf{T}) : \mathbf{S}^{\alpha} \tag{12}$$

where ':' denotes the inner product of second-order tensors defined as $\mathbf{A} : \mathbf{B} = A_{ij}B_{ij}$. Eqn. (12) is derivable by equating the plastic part of the internal mechanical power to the power expended in crystallographic shearing of slip system α with resolved shear stress τ^{α} and shearing rate $\dot{\gamma}^{\alpha}$. The second Piola-Kirchoff stress in the intermediate configuration is linked to the elastic Green-Lagrange strain as follows

$$\mathbf{T} = \mathcal{L} \cdot \mathbf{E}^e = \frac{1}{2}\mathcal{L} \cdot (\mathbf{F}^{eT}\mathbf{F}^e - \mathbf{I}) \tag{13}$$

where $\mathbf{E}^e$ is the elastic Green-Lagrange strain tensor, $\mathcal{L}$ is the elastic stiffness (a fourth-order tensor) and $\mathbf{I}$ is the second-order identity tensor. '·' denotes the product between a fourth-order tensor and second-order tensor to furnish a resultant second-order tensor, defined as $(\mathcal{L} \cdot \mathbf{A})_{ij} = \mathcal{L}_{ijkl}A_{kl}$. We additionally note that the Cauchy stress, $\boldsymbol{\sigma}$, and the first Piola-Kirchoff stress in the reference configuration, $\mathbf{P}$, can be computed from $\mathbf{T}$ as follows:

$$\mathbf{T} = \mathbf{F}^{e-1}\mathbf{P}\,\mathbf{F}^T\mathbf{F}^{e-T} = \det(\mathbf{F}^e)\mathbf{F}^{e-1}\boldsymbol{\sigma}\,\mathbf{F}^{e-T} \tag{14}$$

Finally, the evolution of slip resistance for slip system α, which governs isotropic hardening, is defined as follows [45]:

$$\dot{s}^\alpha = \sum_\beta h^{\alpha\beta}\dot{\gamma}^\beta \tag{15}$$

where $h^{\alpha\beta}$, denotes the hardening rate on slip system α due to the slip-on system β. The hardening moduli $h^{\alpha\beta}$ are prescribed as a power-law relationship involving the combined effect of work hardening and recovery, with both self and latent hardening contributions as follows:

$$h^{\alpha\beta} = \begin{cases} h_0^\beta\left[1 - \dfrac{s^\beta}{s_s^\beta}\right]^{a^\beta} & ;\ \text{coplanar systems} \\[4mm] h_0^\beta q\left[1 - \dfrac{s^\beta}{s_s^\beta}\right]^{a^\beta} & ;\ \text{otherwise} \end{cases} \tag{16}$$

where h_0^β denotes the hardening parameter for slip system β, q is the latent hardening ratio, s_s^β is the saturation slip resistance for slip system β, and a^β is a material constant for slip system β governing the sensitivity of the hardening moduli to the slip resistance.

The constitutive model is implemented in the PRISMS-Plasticity CPFE code, an open-source, scalable software framework to simulate elasto-plastic boundary value problems [35, 46] using the finite element method. In the interest of being succinct, only the constitutive model has been outlined here. For detailed derivations including the incremental constitutive update scheme and derivation of an algorithmic tangent modulus, the reader is referred to previous work [47].

2.2.3   Constitutive Model Calibration

The crystal plasticity constitutive model parameters are obtained by matching the stress-strain curves between simulations and experiments for Mg-4Al samples for two scenarios. Figs. 5(a)-5(b) depict the pole figures corresponding to the samples from these scenarios along with the sample reference frame x-y-z. In the first scenario, the sample was subject to uniaxial tension along the y-direction (Figure 5(a)), deformed up to a strain of approximately 2.5%. In the second scenario, the sample was subject to uniaxial tension along the z-direction (Figure 5(b)), deformed up to a strain of approximately 0.6%. For the simulations, cubical synthetic microstructures were generated using DREAM.3D [48] using the respective textures. For both the cases, 60x60x60 voxelated microstructures containing approximately 2000 grains were instantiated, with the cube length set to L = 500 μm. The cubes were subject to symmetry boundary conditions, depicted in Figs. 5(c)-5(e), where u_0 denotes the maximum displacement applied to the face subject to non-zero displacement boundary condition, similar to the experiment. For the first scenario, u_0 was set to 10 μm(0.025 x L), while for the second scenario u_0 was set to 3 μm(0.006 x L). These

match the approximate macroscopic strain levels that the samples were subject to in the experiments.

All crystal plasticity simulations were performed assuming possible activity of 12 slip systems - 3 basal, 3 prismatic, 6 pyramidal <c+a> - and 6 pyramidal <c+a> twin systems. Figure 5(f) and Figure 5(g) depict the comparison between the stress-strain curves from CPFE simulations and experiments for the first and second scenario, respectively, showing a satisfactory match in the plastic regime for the strain regimes considered. Table 2 lists the elastic stiffness constants used in calibration [49-51] and Table 3 lists the crystal plasticity constitutive model parameters obtained post-calibration. In the hardening law, the latent hardening coefficient was set to $q = 1.0$, while the flow rule parameters were set as $\dot{\gamma}_0 = 0.001$ and $m = 34$.

2.2.4   Grain Boundary Neighborhood Simulations

To construct grain boundary descriptors through which a relationship can be drawn to the micro-Hall-Petch coefficient, some information about the slip activity in the grains is necessary. By virtue of capturing the resolved stress ahead of the blocked slip band, the slip system in the adjacent grain which could potentially accommodate slip transmission, is not known. In the grain containing the slip band, the slip trace and crystallographic orientation can be used to infer the slip system corresponding to that slip band (incoming slip system). To find the slip system that could potentially accommodate slip transmission (potential outgoing slip system), crystal plasticity simulations are employed.

To accomplish this, for each grain boundary case studied, a rectangular region around this grain boundary is identified (Figure 6(a)), which contains the grains sharing this boundary and some of their neighbors. The approximate coordinates of the center of the notch and its length are identified (Figure 6(b)). This information is then used to create a rectangular geometry of the region of interest, with the notch approximated as an ellipse with the same center as that of the notch and major axis length equal to the length of the notch. The minor axis length of the ellipse is set to 1 μm. This microstructure section (a 2D section) is then meshed using 4-node quadrilateral elements via the functionality of Gmsh [52], an open-source 3D finite element mesh generator (Figure 6(d)). The elements are then assigned an identifier corresponding to whichever grain they constitute in the original microstructure (Figure 6(c)). Finally, since we are simulating three-dimensional geometries using our CPFE framework, the 2D microstructure section is extruded along the third direction to create a slice of the microstructure, where the 4-node quadrilateral elements now turn to 8-node brick elements.

Then each microstructure section was subjected to deformation via two boundary conditions:

(i) **Boundary Condition 1** – For the four lateral boundaries (x=0, x=L_x, y=0, y=L_y), the x and y components of displacements were enforced based on a constant velocity gradient representative of uniaxial tension along the x-direction.

$$\mathbf{L} = \dot{\mathbf{F}}\mathbf{F}^{-1}, \ \ \mathbf{F}(0) = \mathbf{I} \ \Rightarrow \ \mathbf{F} = \exp(t\mathbf{L}) \ ; \ \mathbf{L} = \begin{bmatrix} 1 & 0 & 0 \\ 0 & -0.5 & 0 \\ 0 & 0 & -0.5 \end{bmatrix} \tag{17}$$

$$u_x = F_{11}x + F_{12}y + F_{13}z \ , u_y = F_{21}x + F_{22}y + F_{23}z$$

where **F** is the time-dependent deformation gradient, **L** is the constant velocity gradient, t is the time, and u_x and u_y are the x and y components of the

displacement, respectively. The face z-displacement of the face $z = 0$ is set to 0 while the opposite face is treated as a traction-free surface.

(ii)   **Boundary Condition 2**: Symmetry boundary conditions are enforced. The surfaces x=0, y=0 and z=0, respectively, are constrained from displacing along the direction perpendicular to corresponding faces. The surfaces y = L_y and z = L_z are traction free while the face x = L_x is displaced along the x-direction by the amount u_0.

Two sets of boundary conditions were chosen as possible portrayals of tension along x-direction, since the true deformation of the microstructural boundary is not available. Microstructure slices in the simulations strained to about 2% along the x-direction so that the grains under investigation show some slip activity in order to identify the potential outgoing slip system in the grain blocking the slip band. We choose this to be the slip system with the highest accumulated slip in the neighborhood of the slip trace-grain boundary intersection once the deformation of the microstructure section is complete.

Table 2: Elastic stiffness constants (in GPa) for Mg-4Al alloy [49-51]

C_{11}	C_{33}	C_{12}	C_{13}	C_{44}
59.4	61.6	25.61	21.44	16.4

Table 3: Crystal plasticity constitutive model parameters post-calibration

| Mode	s_0^α	h_0^α	s_s^α	a^α
Basal <a>	10.0	0.0	-	1.0
Prismatic <a>	78.0	1000.0	150.0	1.0
Pyramidal <c + a>	140.0	0.0	-	1.0
Twin <c + a>	18.0	0.0	-	1.0
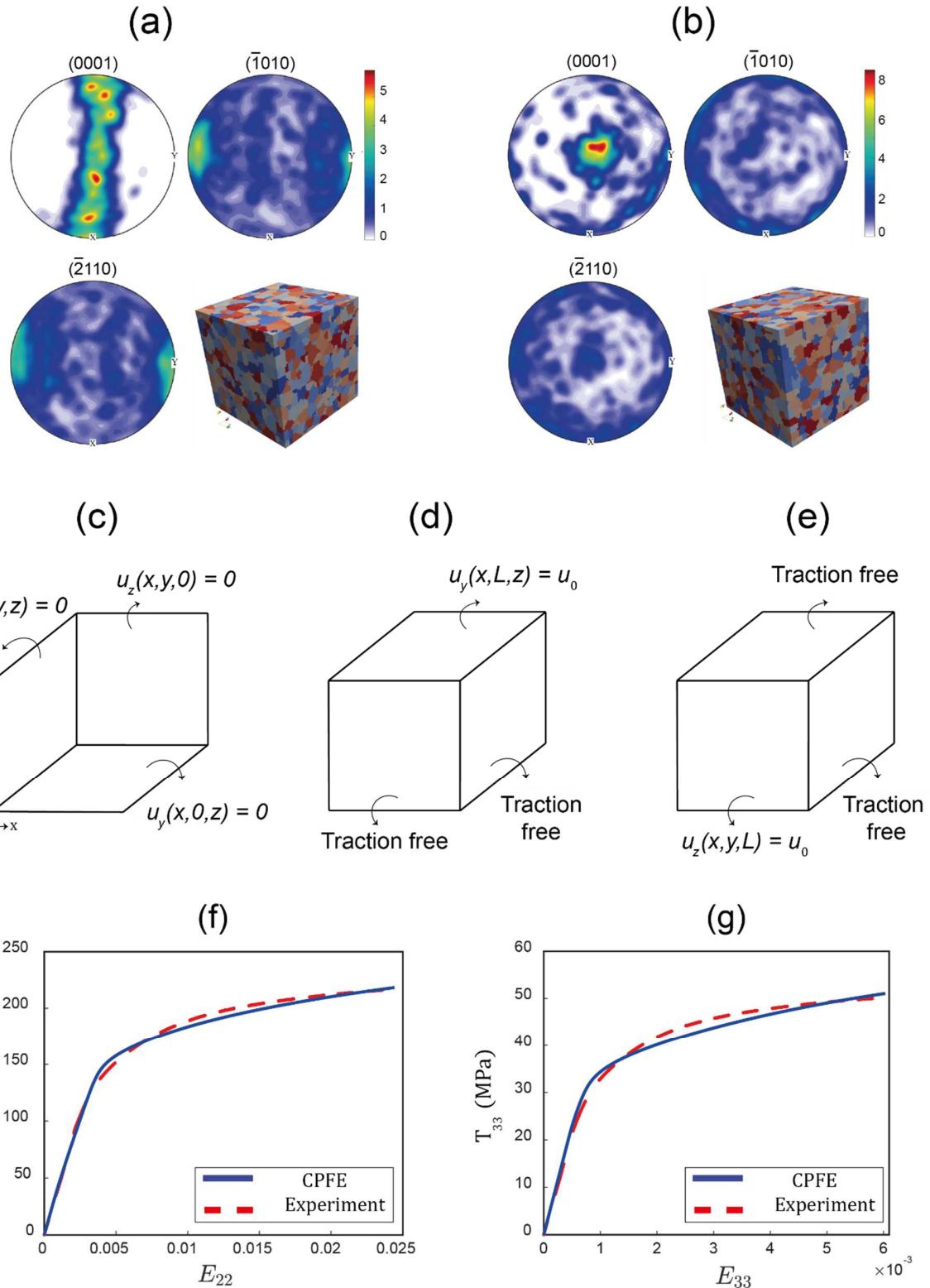
Figure 5: a) Pole figures and synthetic microstructure for first scenario, (b) Pole figures and synthetic microstructure for second scenario, (c) Faces at x=0, y=0 and z=0 enforced as flat

surfaces, (d) Deformation boundary condition for first scenario, (e) Deformation boundary condition for second scenario, (f) Stress-strain curve comparison between CPFE and experiments for the first scenario, and (g) Stress-strain curve comparison between CPFE and experiments for the second scenario.
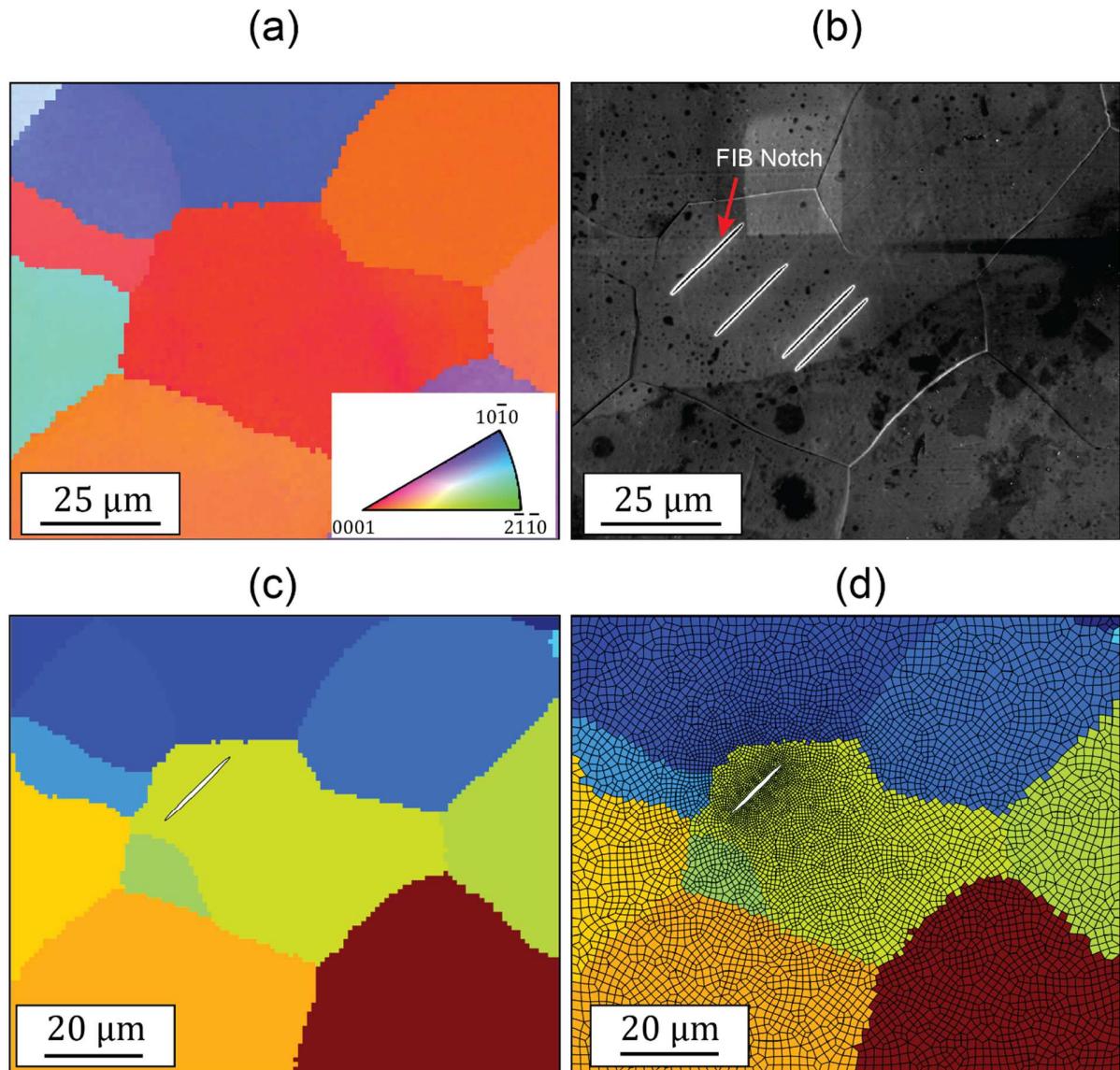

Figure 6: (a) EBSD section for the region around grain boundary, (b) Grain with notch generated using FIB, (c) Grain identifiers for microstructure section, and (d) Microstructure section meshed using Gmsh with 4-node quadrilateral elements with grain identifiers assigned.
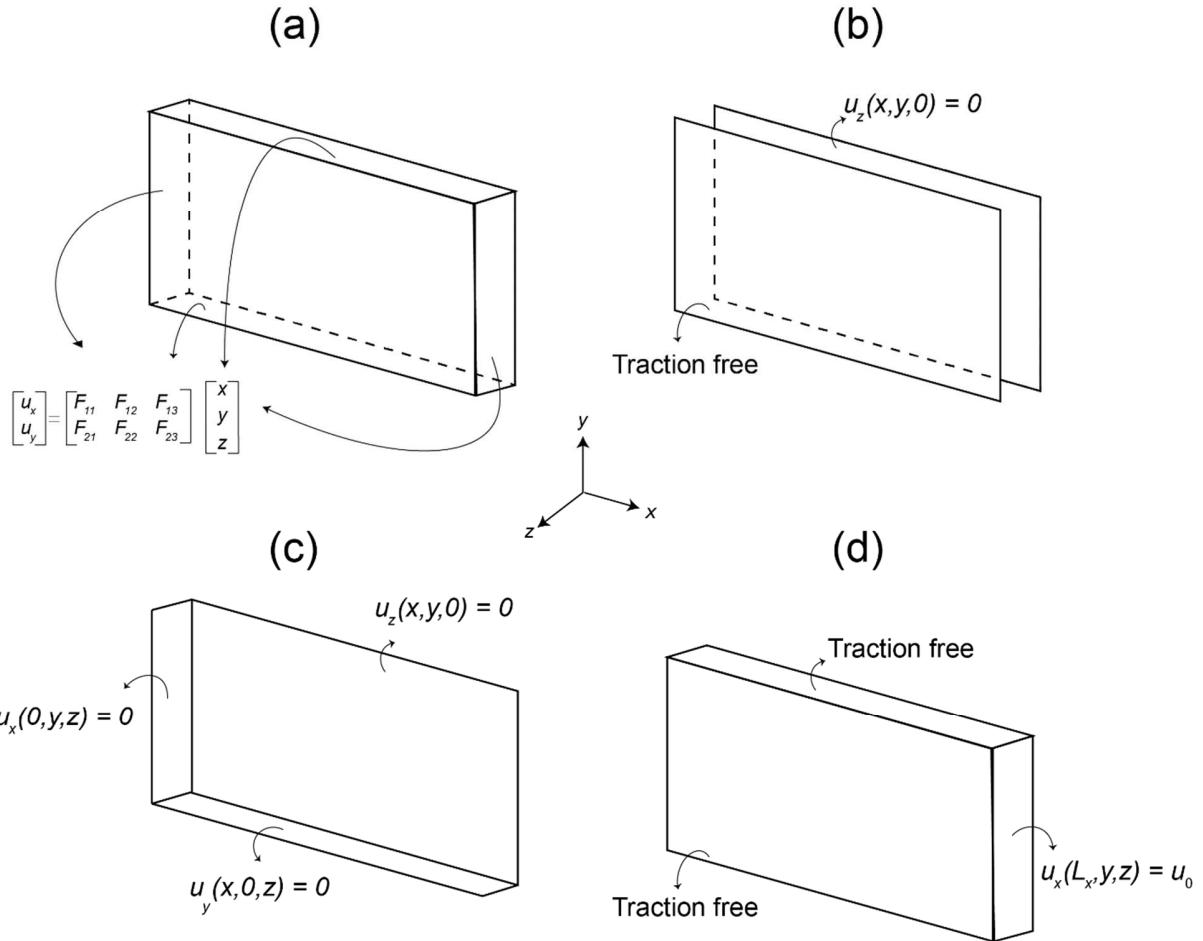
Figure 7: Boundary condition 1 (BC#1): (a) x and y displacement components set on lateral surfaces, (b) x-y plane constrained along z-direction, Boundary condition 2 (BC#2): (c), (d) denote symmetry boundary conditions similar to the boundary condition enforced in the calibration section for scenario 1.

3   Results

3.1   Micro-Hall-Petch Coefficient Calculation

Grain boundaries that block the slip bands generated from the micro-notches are found using SEM, as shown in Figure 3(c) (GB#1). HR-EBSD scans around the interaction zones are captured and the full elastic stress tensor is calculated in the sample. An example of the full tensor map of the stress concentration ahead of a blocked slip band measured by HR-EBSD is shown in Figure 8. More details on how to measure stress components by HR-EBSD are discussed in the previous studies [53, 54]. As it can be seen from Figure 8, the stress induced by the blocked slip band at the grain boundary is revealed most clearly in the σ_{11} and σ_{22} stress components.
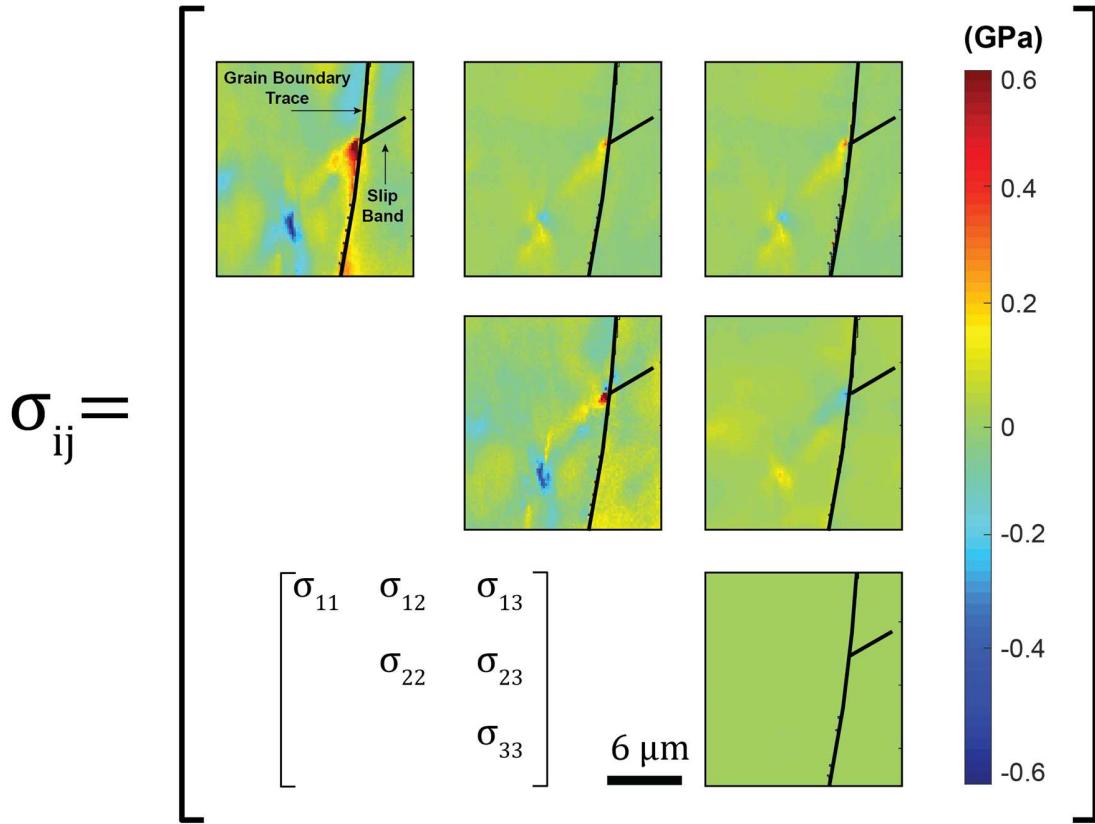
Figure 8: An example of full stress tensor measured in the sample frame by HR-EBSD for a slip band blocked at Grain Boundary 1 (Note: these images are rotated 180 degrees from Figure 3).

The stress tensors in the sample frame are then resolved onto the active slip system of the deformed grain determined by methods explained in section 2.2.4. Figure 9(a) shows an example of the resolved shear stress derived by rotation of stress tensor shown in Figure 8 to another axis system $x_1^r x_2^r x_3^r$, where x_1^r, x_3^r, and x_2^r are along the slip plane normal, Burgers vectors, and the direction perpendicular to the Burgers vector on the slip plane of the active slip system, respectively.

Stress values ahead of the pile up is extracted along with the slip band in the undeformed grain, indicated by X direction in Figure 9(a). The stress values are compared with the dislocation pile-up model given by Eqn. 6 as shown in Figure 9(b). The experimental data shows the same trend as the theoretical model. The micro-Hall-Petch coefficients k_μ^α, for all seven grain boundaries are estimated by fitting the experimental data with the dislocation pile-up model, and the results are presented in Table 4. The slip system level grain sizes in the deformed grains and the micro-notch sizes for each grain boundary are also reported in Table 4.
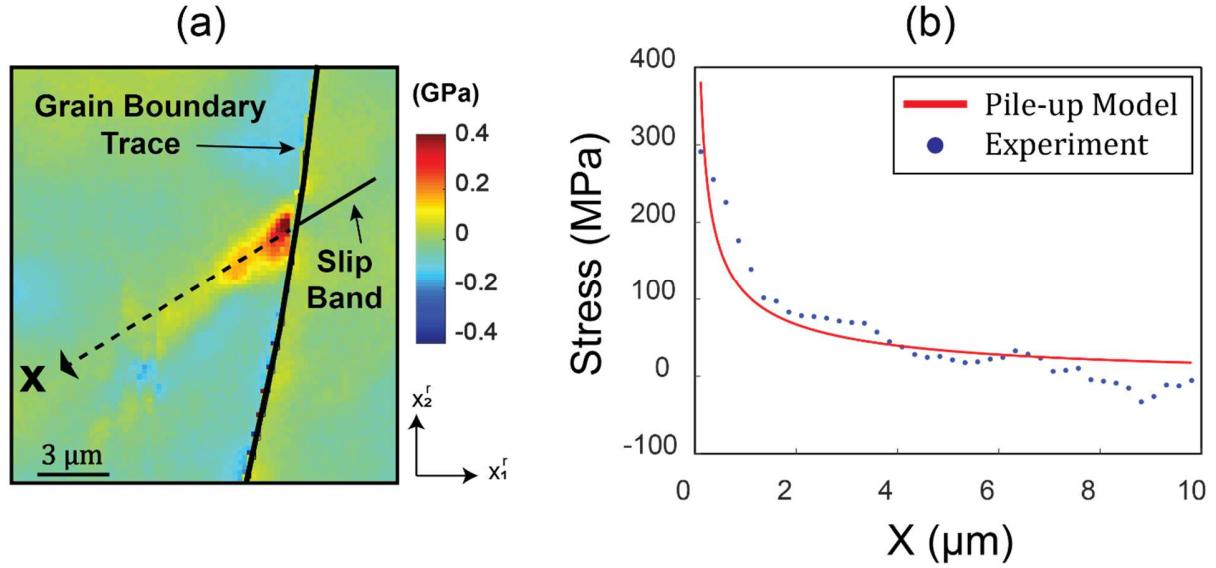
Figure 9: (a) HR-EBSD stress map of the resolved shear stress on the active slip system in the right grain. The active slip system is defined based on the trace analysis and CPFE. The observed stress profile in front of the pile-up is extracted along the dashed line and compared with the pile-up model. (b) The comparison of resolved shear stress ahead of pile up was measured by HR-EBSD and the pile-up model (Eqn. 6) to assess the prismatic micro-Hall-Petch slope in different GBs.

Table 4: A list of the prismatic micro-Hall-Petch coefficient for different GBs

GB Number	1	2	3	4	5	6	7
Slip Level Grain Size in the Grain with Slip Band (μm)	40	40	39	44	41	41	41
Notch Size (μm)	20	20	19	21	18	17	17
$k_\mu^{prismatic}$ (**MPa. m$^{1/2}$**)	0.455	0.618	0.661	0.635	0.685	0.138	0.641
	±	±	±	±	±	±	±

	0.05	0.06	0.07	0.07	0.02	0.02	0.07

3.2 Grain Boundary Parameters

To understand the effect of grain boundary parameters on micro-Hall-Petch coefficient, the quantitative geometrical angles describing the slip transmission across grain boundary as shown in Figure 10 need to be determined. To achieve this goal (3.2.1), the grain boundary plane orientation angles are measured, and (3.2.2) the active slip systems in Grain 1 (grain with the slip band, Grain 1 in Figure 3c) and Grain 2 (grain without evidence of any slip band, Grain 2 in Figure 3c) are determined.
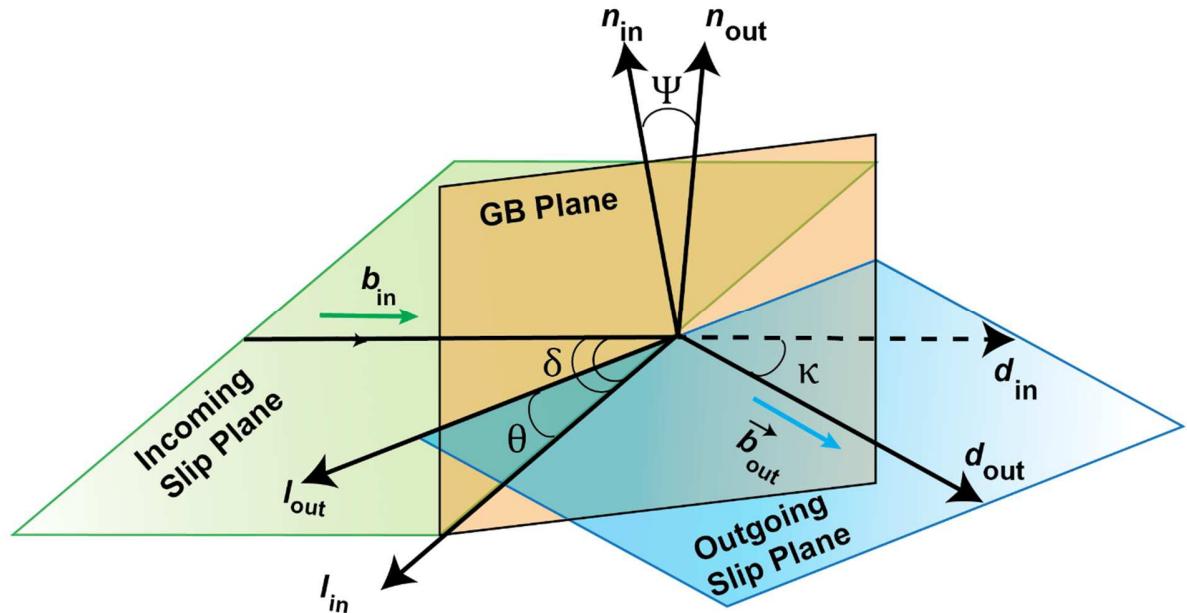
Figure 10. A schematic representative for slip transmission through a GB. $\vec{b}_{in}$: Burgers vector of the incoming slip system, $\vec{b}_{out}$: Burgers vector of the outgoing slip system, $\vec{n}_{in}$: Slip plane normal of the incoming slip system, $\vec{n}_{out}$: Slip plane normal of the outgoing slip system, $\vec{l}_{in}$:

Intersection line of the incoming slip plane and GB, $\vec{l}_{out}$: Intersection line of the outgoing slip plane and GB, $\vec{d}_{in}$: Slip direction of the incoming slip system, $\vec{d}_{out}$: Slip direction of the outgoing slip system, θ: Angle between the two slip plane traces on the grain boundary plane, κ: Angle between slip directions, ψ: Angle between slip plane normal, δ: Angle between the incoming slip direction and the incoming slip plane trace on the grain boundary plane.

3.2.1 Grain Boundary Plane Orientation Angles Measurement

The GB plane orientation angles include the *trace* angle (α), defined as the angle between the loading direction and the trace of the GB plane on the sample surface, and the grain boundary *plane* angle (β), defined as the angle between the sample surface normal and the trace of the GB plane (Figure 11(a)). α can be manually assessed using the plan view image captured by scanning electron microscopy (SEM), as shown in Figure 11(b). It is worth noting that x_1-direction in the plane view image should be aligned with the loading axis. Cross-sectional analysis of the grain boundary is performed to obtain the grain boundary plane angle, as shown in Figure 11(c). A focused ion beam (FIB) is used to lift out a region of material perpendicular to the grain boundary line on the sample surface, and the angle β is manually measured for the different GBs. Table 5 summarizes the measured α and β angles for the seven different GBs studied in this work.
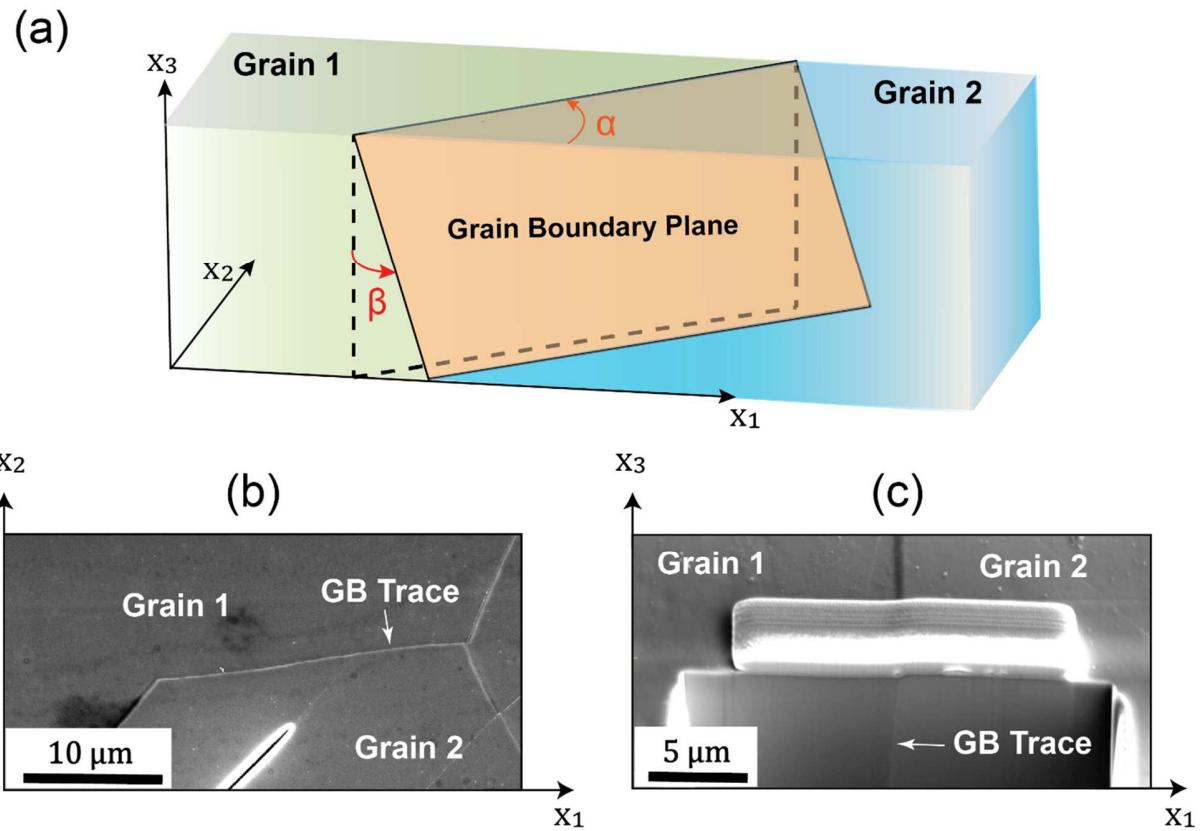
Figure 11: (a) Schematic representation of the GB plane. (c) The GB trace angle (α) is measured using the GB's plan view image (SEM image). (e) The GB plane angle (β) is measured using a cross-section of the GB after FIB removal of adjacent material.

Table 5: List of the trace angle (α) and the plane angle (β) of the different GBs investigated in this study

GB ID	1	2	3	4	5	6	7
α (°)	176.18	113.03	10.71	149.23	102.42	73.67	7.41
β (°)	127.35	87.16	55.16	62.26	49.34	76.96	90.11

3.2.2 Grain neighborhood simulations

Simulations were conducted on GB neighborhoods for seven GB cases with two boundary conditions, as described in Section 2.2.4. Figure 12 depicts the variation of accumulated slip for the 3 basal and 3 prismatic slip systems for a particular GB neighborhood represented by the microstructure in Figure 6, for BC#1. As expected, profuse basal slip is observed in most regions of the microstructure section, and particularly in the grains not containing the notch. It is interesting to observe significant prismatic slip (relative to basal slip) in the grain containing a notch close to both notch ends. This affirms to some extent the experimental observation of a slip band emanating from the notch coincident with the trace of a prismatic plane, parallel to the trace of the notch. In this particular case, the alignment of the notch corresponds to that of the $[1\bar{2}10](10\bar{1}0)$ prismatic system. Figure 12(d) depicts the accumulated slip variation of the $[1\bar{2}10](10\bar{1}0)$ prismatic system, where a diffuse localization of accumulated slip can be observed. This could perhaps denote a representation of sharper slip localization observed in the experiment since one of the directions in which the accumulated slip localizes in the simulations is parallel to the trace of the notch. Figure 14(a) is a discrete map denoting the slip system ID (Table 6) with the most accumulated slip at each element of the FE mesh, with Figure 14(b) zooming in on the region around the notch from which the slip band emanates. The dominance of $[1\bar{2}10](10\bar{1}0)$ prismatic activity is apparent.

Figure 13 depicts the variation of accumulated slip for the 3 basal and 3 prismatic slip systems of the same microstructure for BC#2, where one can observe more profuse basal slip and relatively lower prismatic slip in the microstructure as compared to BC#1. However, it continues to demonstrate significant prismatic slip activity close to the notch, particularly for the $[1\bar{2}10](10\bar{1}0)$ prismatic system. Figure 14(c) is a discrete map denoting the slip system ID with

the most accumulated slip at each element of the FE mesh for BC#2, with Figure 14(b) zooming in on the region around the notch from which the slip band emanates. The conclusions remain the same as for BC#1, with the $[1\bar{2}10](10\bar{1}0)$ prismatic system being dominant in terms of accumulated slip.

Another interesting observation is the activation of all the prismatic systems in the vicinity of the notch for both boundary conditions (Figure 14(b) and 14(d)), irrespective of the direction of the notch. This is most likely caused by significant changes in the in-plane stress state around the notch due to the combined effect of the traction-free boundary and notch curvature. This entire exercise essentially demonstrates the effectiveness of such simple crystal plasticity models in predicting slip localizations in agreement with experimental observations. Additionally, it showcases the need to simulate only a very local neighborhood of the GB (about 10 grains) to make these predictions which are noteworthy considering performing inexpensive simulations which garner essential information.

The slip system ID map in Figure 14 is now used to obtain the potential outgoing slip system. In this case, the potential outgoing slip system is chosen as the one with the most accumulated slip in the vicinity of the slip trace-GB intersection (Figure 14(b) and 14(d)). For the present case, the neighborhood of this intersection for BC#1 presents two possibilities – slip system ID 2 and 3. In case of multiple possibilities, the slip system representing the majority of the grain in the slip system ID map is chosen, which in this case is ID 2. Similarly, slip system ID 2 is considered the potential outgoing slip system for BC#2 as well. Table 7 lists the incoming slip system (from slip trace) and potential outgoing slip system predicted by CPFE, along with some of the relevant angles characterizing the GB and the slip system-GB pair.

Table 6: List of slip direction and slip plane orientations for different slip/twin systems for Mg alloys.

| Slip/Twin System	ID	Slip Direction	Slip Plane
Basal	1	$[11\bar{2}0]$	(0001)
	2	$[\bar{2}110]$	(0001)
	3	$[1\bar{2}10]$	(0001)
Prismatic<a>	4	$[1\bar{2}10]$	$(10\bar{1}0)$
	5	$[2\bar{1}\bar{1}0]$	$(01\bar{1}0)$
	6	$[11\bar{2}0]$	$(\bar{1}100)$
Pyramidal<c+a>	7	$[\bar{1}\bar{1}23]$	$(11\bar{2}2)$
	8	$[1\bar{2}13]$	$(\bar{1}2\bar{1}2)$
	9	$[2\bar{1}\bar{1}3]$	$(\bar{2}112)$
	10	$[11\bar{2}3]$	$(\bar{1}\bar{1}22)$
	11	$[\bar{1}2\bar{1}3]$	$(1\bar{2}12)$
	12	$[\bar{2}113]$	$(2\bar{1}\bar{1}2)$
Twin<c + a>	13	$[\bar{1}011]$	$(10\bar{1}2)$
	14	$[10\bar{1}1]$	$(\bar{1}012)$
	15	$[\bar{1}101]$	$(1\bar{1}02)$
	16	$[1\bar{1}01]$	$(\bar{1}102)$
	17	$[0\bar{1}11]$	$(01\bar{1}2)$
	18	$[01\bar{1}1]$	$(0\bar{1}12)$
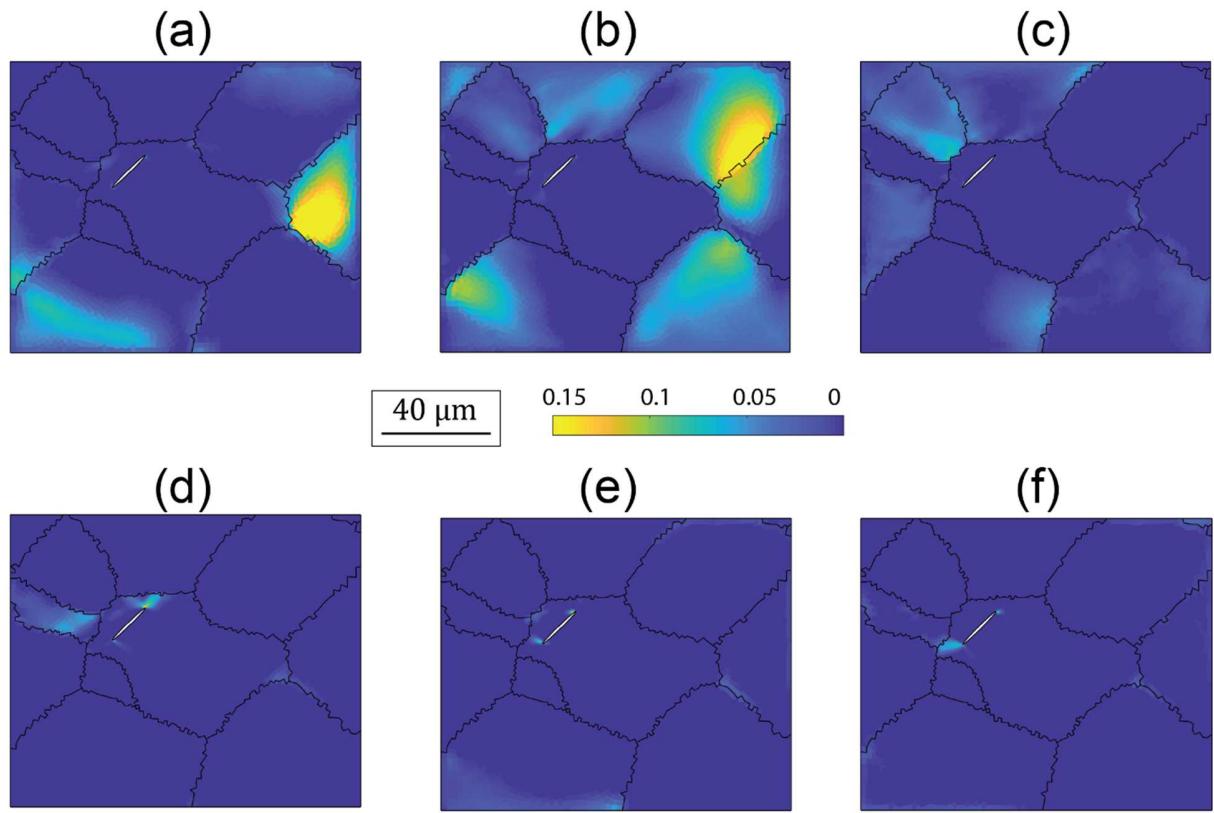
Figure 12. Boundary Condition 1: (a) Accumulated slip for Basal 1, (b) Accumulated slip for Basal 2, (c) Accumulated slip for Basal 3, (d) Accumulated slip for Prismatic 1, (e) Accumulated slip for Prismatic 2, and (f) Accumulated slip for Prismatic 3. It can be observed that prismatic slip is particularly dominant in the neighborhood of the notches on either side.
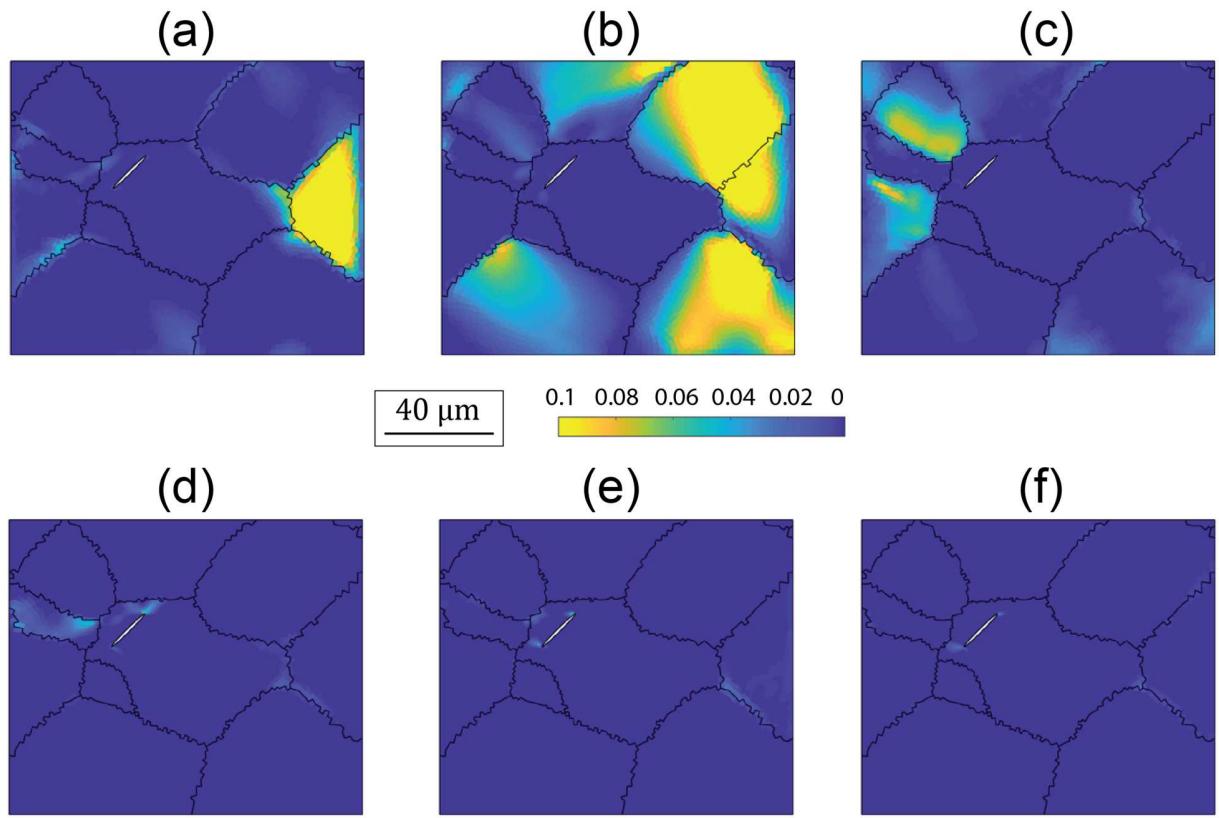
Figure 13. Boundary Condition 2: (a) Accumulated slip for Basal 1, (b) Accumulated slip for Basal 2, (c) Accumulated slip for Basal 3, (d) Accumulated slip for Prismatic 1, (e) Accumulated slip for Prismatic 2, and (f) Accumulated slip for Prismatic 3. It can be observed that prismatic slip is particularly dominant in the neighborhood of the notches on either side.
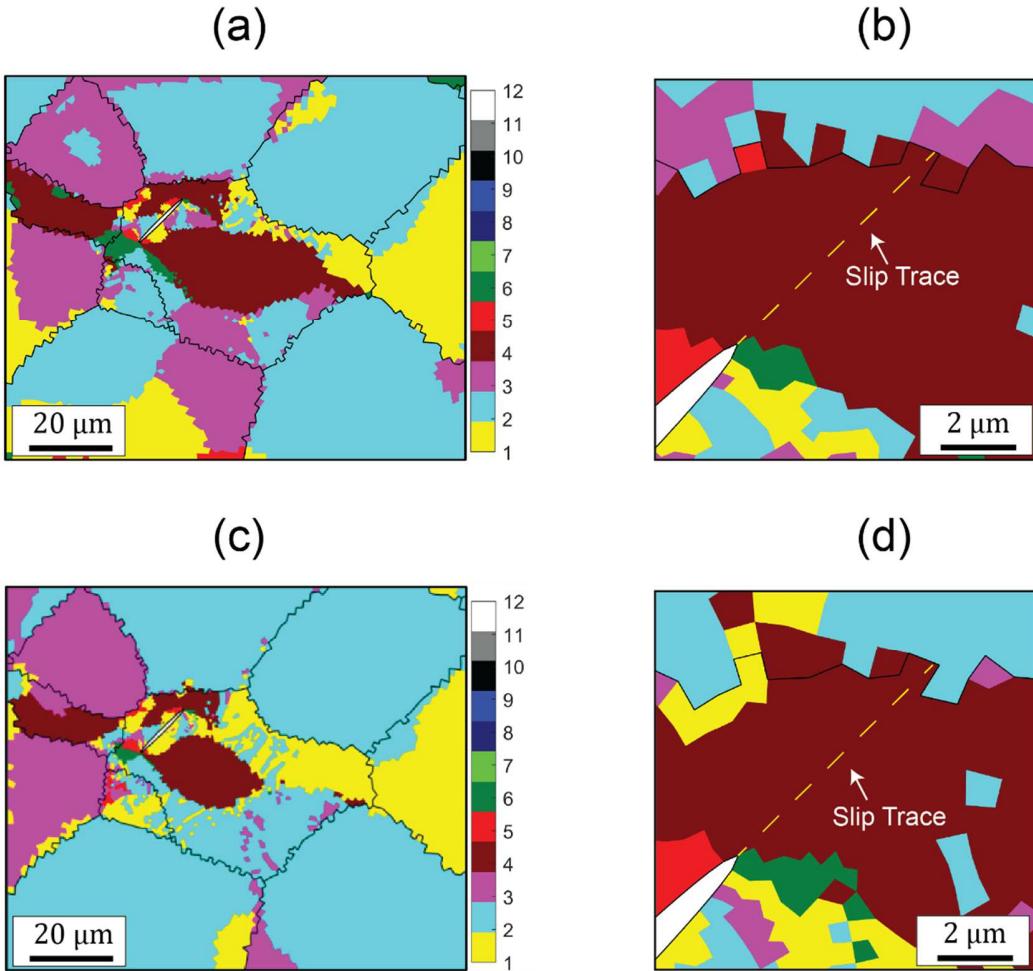
Figure 14: Visualization of most active slip system for all elements of the microstructure, corresponding to GB ID 3, included in Table 7. The numbers in the color bar correspond to the slip system IDs in Table 6. The most active slip system in every element is recognized as the one with the highest accumulated slip within the element. The basal and prismatic <a> slip systems dominate in slip activity for both boundary conditions considered. (a) BC#1 – Most active slip system map (b) Close-up with prismatic slip trace superposed, (c) BC#2 – Most active slip system map (d) Close-up with prismatic slip trace superposed. For both BC#1 and BC#2, the incoming slip system is $(10\bar{1}0)[1\bar{2}10]$ and the potential outgoing slip system is $(0001)[\bar{2}110]$.

3.3 Estimation of micro-Hall-Petch Coefficient as a Function of Grain-Boundary Parameters

Table 7 and Table 8 summarize the slip systems of the observed prismatic slip band generated from the micro-notch and the potential outgoing slip systems under BC#1 and BC#2 for each individual grain boundary, respectively. The relevant angles (θ, κ, ψ, δ) are calculated and listed in these tables for each GB case.

Table 7: List of the incoming prismatic slip system and the potential outgoing slip system of each grain boundary under BC#1, and the relevant angles (θ,κ,ψ, δ) describing the prismatic slip band interaction with each grain boundary.

GB ID	Incoming Slip System	Potential Outgoing Slip System	θ (°)	κ (°)	ψ (°)	δ (°)
1	$(01\bar{1}0)[2\bar{1}\bar{1}0]$	$(0001)[\bar{2}110]$	74.73	69.94	63.26	27.48
2	$(01\bar{1}0)[2\bar{1}\bar{1}0]$	$(10\bar{1}0)[1\bar{2}10]$	65.74	88.33	88.35	9.64
3	$(10\bar{1}0)[1\bar{2}10]$	$(0001)[\bar{2}110]$	80.95	70.06	65.53	26.67
4	$(\bar{1}100)[11\bar{2}0]$	$(0001)[1\bar{2}10]$	79.26	42.34	53.72	49.29
5	$(10\bar{1}0)[1\bar{2}10]$	$(0001)[11\bar{2}0]$	47.36	36.59	40.92	59.65
6	$(01\bar{1}0)[2\bar{1}\bar{1}0]$	$(01\bar{1}0)[2\bar{1}\bar{1}0]$	43.92	31.10	22.73	86.94
7	$(01\bar{1}0)[2\bar{1}\bar{1}0]$	$(0001)[\bar{2}110]$	87.95	70.54	72.79	58.48

Table 8: List of the incoming prismatic slip system and the potential outgoing slip system of each grain boundary under BC#2, and the relevant angles (θ,κ,ψ, δ) describing the prismatic slip band interaction with each grain boundary.

GB ID	Incoming Slip System	Potential Outgoing Slip System	θ (°)	κ (°)	ψ (°)	δ (°)
1	$(01\bar{1}0)[2\bar{1}\bar{1}0]$	$(0001)[\bar{2}110]$	65.89	69.94	63.26	27.48
2	$(01\bar{1}0)[2\bar{1}\bar{1}0]$	$(10\bar{1}0)[1\bar{2}10]$	70.22	88.33	88.35	9.64
3	$(10\bar{1}0)[1\bar{2}10]$	$(0001)[\bar{2}110]$	80.95	70.06	65.53	26.67
4	$(\bar{1}100)[11\bar{2}0]$	$(0001)[\bar{2}110]$	79.26	59.01	53.72	49.29
5	$(10\bar{1}0)[1\bar{2}10]$	$(0001)[1\bar{2}10]$	47.36	47.53	40.92	59.65
6	$(01\bar{1}0)[2\bar{1}\bar{1}0]$	$(01\bar{1}0)[2\bar{1}\bar{1}0]$	43.92	31.10	22.73	86.94
7	$(01\bar{1}0)[2\bar{1}\bar{1}0]$	$(0001)[\bar{2}110]$	87.95	70.54	72.79	58.48

The prismatic micro-Hall-Petch coefficient values (Table 4) are plotted versus the corresponding θ, the angle between the two slip plane traces on the grain boundary plane (Figure 15(a) for BC#1, Figure 16(a) for BC#2); versus κ, the angle between incoming and outgoing slip directions (Figure 15(b) for BC#1, Figure 16(b) for BC#2); versus δ, the angle between the incoming slip direction and the intersection of the incoming slip plane with the grain boundary plane (Figure 15(c) for BC#1, Figure 16(c) for BC#2); and versus ψ, the angle between slip plane normals (Figure 15(d) for BC#1, Figure 16(d) for BC#2). The coefficient of determination, the R-squared value ($0 < R^2 < 1$), is used to quantify and compare the correlation between each of the geometrical expression angles and the micro-Hall-Petch coefficient (as shown in each plot). The linear regression is stronger at higher values of R^2.
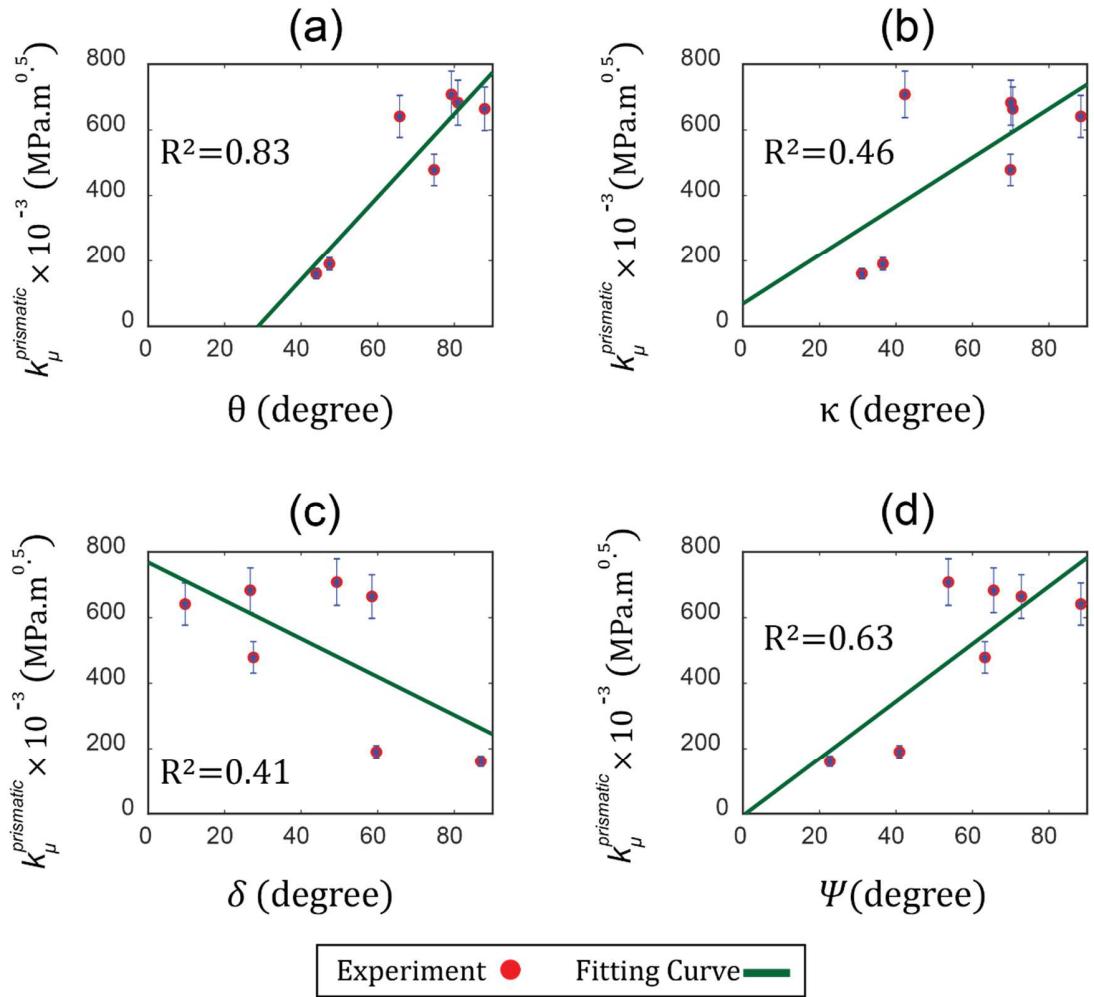
Figure 15: The prismatic micro-Hall-Petch coefficient values relevant angles (θ, κ, ψ, δ) calculated based on BC#1. (a) $k_\mu^{prismatic}$ vs the angle between the two slip plane intersections with the GB (θ). (b) $k_\mu^{prismatic}$ vs the Angle between incoming and outgoing slip directions (κ). (c) $k_\mu^{prismatic}$ vs the angle between slip plane normal (ψ). (d) $k_\mu^{prismatic}$ vs the angle between the incoming slip direction and the incoming slip plane trace on the GB plane (δ).
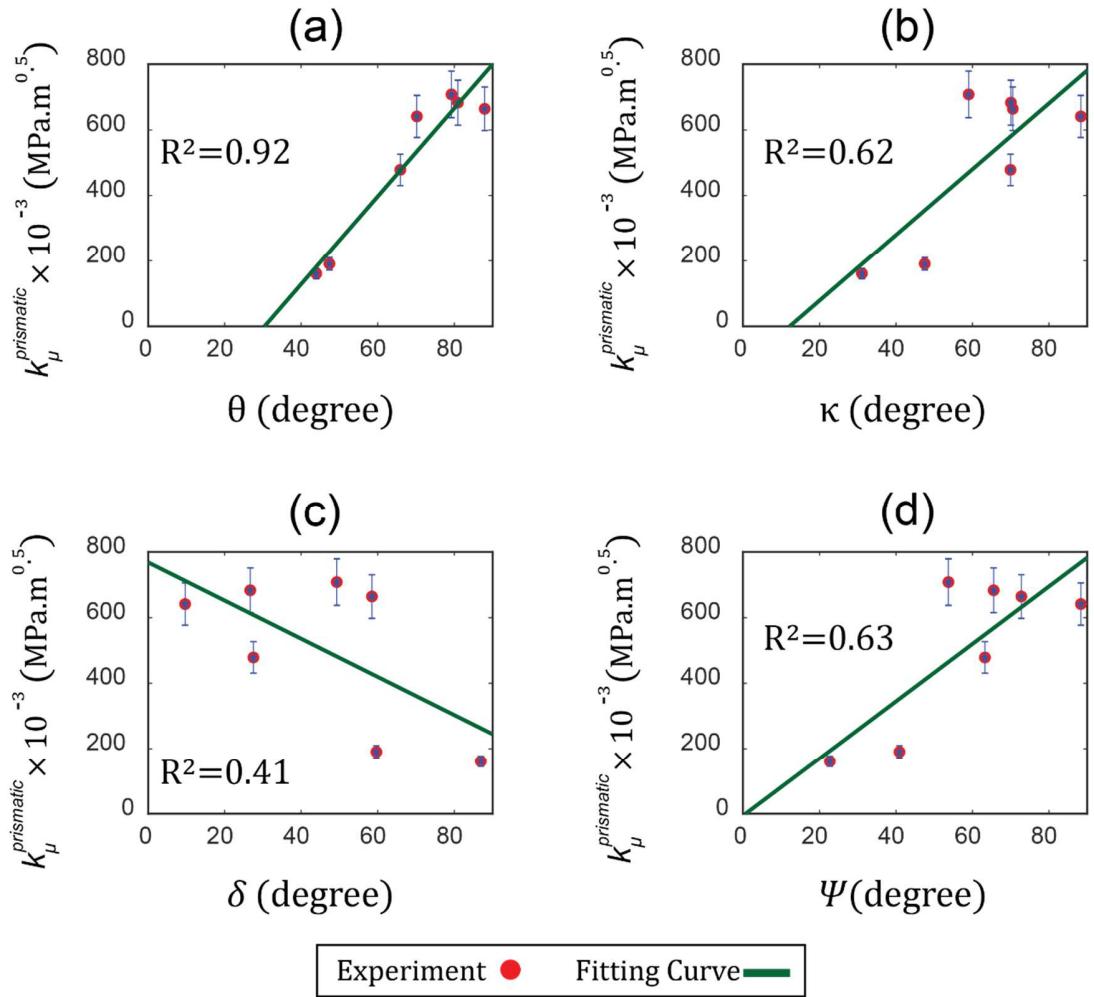
Figure 16: $k_\mu^{prismatic}$ values against relevant angles (θ, κ, ψ, δ) calculated based on BC#2. (a) $k_\mu^{prismatic}$ vs the angle between the two slip plane intersections with the GB (θ). (b) $k_\mu^{prismatic}$ vs the angle between incoming and outgoing slip directions (κ). (c) $k_\mu^{prismatic}$ vs the angle between slip plane normal (ψ). (d) $k_\mu^{prismatic}$ vs the angle between the incoming slip direction and the incoming slip plane trace on the GB plane (δ).

4 Discussion

Prismatic slip band pile-ups at seven different GBs (Table 1) were studied using a combination of HR-EBSD, dislocation pile-up theory, and CPFE simulations. The grains with the highest Schmid factor for the prismatic slip system and the lowest Schmid factor for the basal slip were selected. A series of micro-FIB notches (Figure 3) parallel to the prismatic slip plane was machined in the grains to act as initiation sites for the prismatic slip bands. The resolved shear stress field ahead of the pile-up was measured using HR-EBSD approach (Figure 8), and the resulting stress profiles were fit to the expressions from a dislocation pile-up model to assess the micro-Hall-Petch coefficient for each individual GB (Table 4). The calculated $k_\mu^{prismatic}$ values vary from 0.138 MPa. $m^{1/2}$ to 0.665 MPa. $m^{1/2}$ which are almost three times larger than the calculated values for the k_μ^{basal} (0.054 MPa. $m^{1/2}$ − 0.184 MPa. $m^{1/2}$) [29]. In our phenomenological model, since the applied resolved shear stress equilibrating a pile-up is assumed to be a Hall-Petch type relation, $k_\mu^{prismatic}$ values already subsume the higher critical stress for prismatic slip compared to basal. This expectation is also consistent with experimental Hall-Petch constants for textures with prismatic + basal slip being higher than when primarily basal slip is present [21, 55, 56].

To understand the role of grain boundaries in the observed variation of $k_\mu^{prismatic}$, the relevant angles ($\theta, \kappa, \psi, \delta$) for each individual GB was calculated. First, cross-sectional analysis of the GBs was performed by FIB to provide 3-D insights of the GBs plane, as summarized in Table 5. Then, CPFE modeling of each GB and the surrounding microstructure in the presence of micro-FIB notches under two different boundary conditions were used to predict the potential outgoing slip system (Table 7 and Table 8). The $k_\mu^{prismatic}$ values were plotted against the

relevant geometric quantities involving the angles $(\theta, \kappa, \psi, \delta)$ for both boundary conditions (Figure 15 and Figure 16) and the results are evaluated using R^2 values. In both boundary conditions, the plots of $k_\mu^{prismatic}$ values against the angle between the two slip plane intersections with the GB (θ) have the highest R^2 values (Figure 15(a) and Figure 16(a)), which is implying the critical role of the GB plane in estimating the prismatic micro-Hall-Petch coefficient. A similar observation was reported in our previous work [29], in the case of k_μ^{basal} and its strong correlation with θ. This observation can be interpreted by the model presented by Davis [57] where it was shown that the energy barrier of each individual GB for stepped dislocation formation is proportional to the $\sin(\theta)$.

The angle between the slip directions (κ), which was reported as the second most effective angle in determining basal micro-Hall-Petch in the previous work [29], shows a considerable correlation with $k_\mu^{prismatic}$ values ((Figure 15(b) and Figure 16(b)). It is well known that the magnitude of residual Burgers vectors in slip transmission is proportional to κ angle and uses as a criterion to evaluate the strength of each individual GB against slip transmission [58-61].

Although, the angle between the incoming slip direction and the intersection of the incoming slip plane with the GB plane (δ), and the angle between slip plane normals (ψ), show a correlation with the $k_\mu^{prismatic}$ values ((Figure 15(c), Figure 15(d), Figure 16(c), and Figure 16(d)), they are not as informative about slip transmission and GB as the other two angles. δ does not capture the outgoing slip system and its grain information and ψ does not include any information about grain boundary plane orientations.

To consider both θ and κ angles in the estimation of the $k_\mu^{prismatic}$, the following equation is proposed:

$$k_\mu^{prismatic} = K^{prismatic}(1 - \cos(\theta)\cos(\kappa))^c \; ; c > 0 \tag{18}$$

where $K^{prismatic}$ and c are model parameters. A similar relationship was proposed for the estimation of k_μ^{basal}[29]. The model was proposed based on the slip transmission criteria developed by Lee–Robertson–Birnbaum[62-64], where the factor $\cos(\theta)\cos(\kappa)$ was used to estimate the outgoing slip systems.

$k_\mu^{prismatic}$ values (Table 4) were fit with Equation 18 under both boundary conditions (Figure 17). The model parameters under BC#1 (Table 7) and BC#2 (Table 8) are obtained as $K^{prismatic} = 0.680 \pm 0.07 \, \text{MPa.m}^{1/2}$ and c = 1.55 under BC#1, and $K^{prismatic} = 0.687 \pm 0.07 \, \text{MPa.m}^{1/2}$ and c = 1.83 under BC#2. Substituting Eqn, 18 in Eqn. 5 yields an expression for the slip resistance of prismatic slip systems as follows

$$\tau^{prismatic} = \tau_0^{prismatic} + \frac{K^{prismatic}(1 - \cos(\theta)\cos(\kappa))^c}{\sqrt{2a}} \tag{19}$$

with the effect of texture and microstructural size taken into account. Along with a similar expression proposed for the basal slip in earlier work [29], this provides avenues to capture texture-grain size coupling for Mg alloys. It is worthwhile to note that the entire procedure developed in this work can be extended to any alloy system and is particularly important when there is significant plastic anisotropy arising from the underlying crystallography.
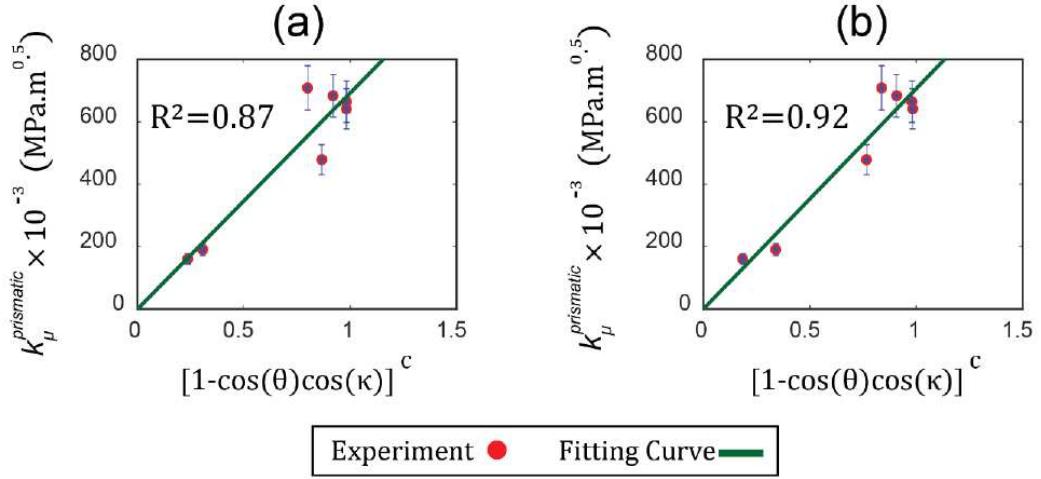
Figure 17: $k_\mu^{prismatic}$ values against $(1 - \cos(\theta)\cos(\kappa))^c$ based on (a) BC#1 and (b) BC#2.

The dependence of the micro-Hall-Petch coefficient for different slip systems on grain boundary metrics can be used as inputs to CPFE simulations, which can simulate the coupling between texture and grain-size effect. It is important to note that these simulations often involve 3-D synthetic microstructures generated based on input statistics which either don't provide grain boundary inclinations due to a voxelated mesh (like in DREAM.3D) or where grain boundary conforming meshes are generated with flat grain boundaries and not curved boundaries(like in Neper). As an alternative, one can use the angles κ and ψ to construct the compatibility factor $\cos(\psi)\cos(\kappa)$. Figure 18 depicts $k_\mu^{prismatic}$ values against $(1 - \cos(\psi)\cos(\kappa))^c$ with $K^{prismatic} = 0.689 \pm 0.07 \, \text{MPa.m}^{1/2}$ and c = 0.85 under BC#1, and $K^{prismatic} = 0.699 \pm 0.07 \, \text{MPa.m}^{1/2}$ and c = 1.07 under BC#2. This functional form can be used in CP modeling where each slip system and material point pair in the microstructure is assigned a slip-system level grain size (calculate from microstructural position data) and micro-Hall-Petch coefficient (using the functional form in Equation 18). This is the subject of study in our upcoming work, where the proposed model is input into a CPFE framework to study texture-grain size coupling.

From the perspective of modeling the microstructural slices, it is to be noted that the slip band is not explicitly modeled, but the stress concentration at the notch is used to naturally initiate prismatic slip in the vicinity. Alternatively, the slip band itself can be explicitly modeled in CPFE using softening-based models [65-67] or using more recent crystal plasticity peridynamics (CPPD) models [68-70] where localizations are a natural consequence of non-local interactions. These approaches can capture the existence of localization bands more in line with experimental observations.
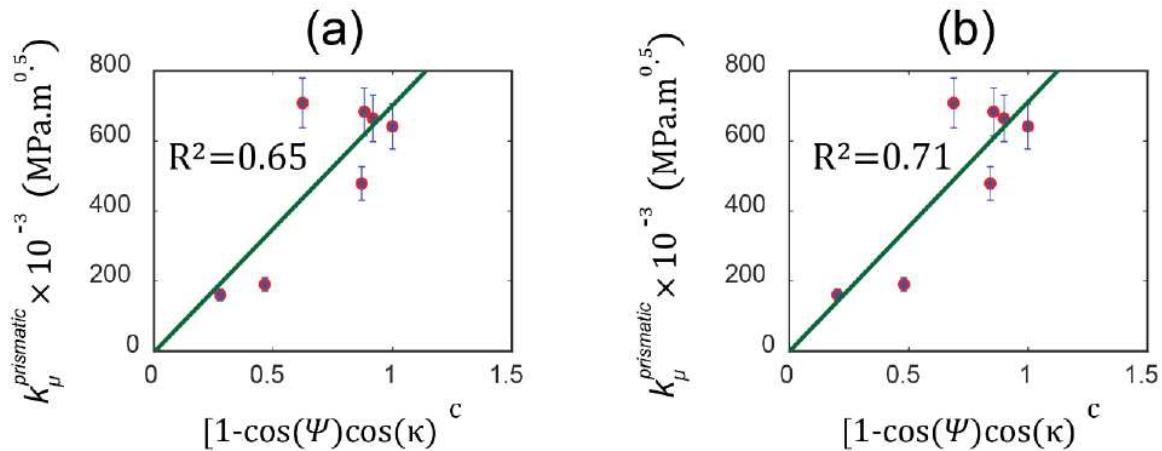
Figure 18: The prismatic slip system micro-Hall-Petch coefficients $\left(k_\mu^{prismatic}\right)$ for the seven-cases are plotted against the factor $(1 - \cos(\psi)\cos(\kappa))^c$ based on (a) BC#1 and (b) BC#2.

5   Conclusions

− An experimental method was developed to initiate the prismatic slip in the form of the localized band at low-stress levels in Mg-4Al. A series of sharp micro-notches parallel to the prismatic slip plane in specific grains were machined to act as slip initiation sites due to stress concentration and subsequent plasticity accommodation in front of a notch.

- A one-dimensional continuum dislocation pile-up model, coupled with the micro-Hall-Petch phenomenological model, was used to estimate the micro-Hall-Petch coefficient for prismatic slip from pile-up stress data.

- The resolved shear stress ahead of blocked prismatic slip bands at seven different grain boundaries in Mg-4Al was measured using HR-EBSD method. The calculated $k_\mu^{prismatic}$ values vary from 0.138 MPa. $m^{1/2}$ to 0.665 MPa. $m^{1/2}$ which are almost three times larger than the calculated values for the k_μ^{basal} (0.054 MPa. $m^{1/2}$ −0.184 MPa. $m^{1/2}$).

- Crystal plasticity simulations of microstructures slices for different GB cases were performed to inform the potential outgoing slip system, required to construct geometric expressions and ascribe $k_\mu^{prismatic}$ values to dependence on these quantities.

- The $k_\mu^{prismatic}$ values were correlated with the geometric descriptors of the GBs, and it was concluded that the angle between the two slip plane traces on the GB plane (θ), and the angle between slip directions (κ) were the two most effective geometric parameters in estimating the magnitude of $k_\mu^{prismatic}$. A relationship, $k_\mu^{prismatic} = K^{prismatic}(1 - \cos(\theta)\cos(\kappa))^c$, was suggested including both of these angles to estimate the slip system level Hall-Petch slope for prismatic slip system, and the model parameters, $K^{prismatic}$ and c, were calibrated for Mg-4Al alloys.

Acknowledgments

Data Availability: The data on which this paper was based is available in Materials Commonsat DOI 10.13011/m3-98qq-sc35 (https://materialscommons.org/public/datasets/182

Reference

[1] M. Easton, A. Beer, M. Barnett, C. Davies, G. Dunlop, Y. Durandet, S. Blacket, T. Hilditch, P. Beggs, Magnesium alloy applications in automotive structures, Jom 60(11) (2008) 57-62.

[2] B. Landkof, Magnesium applications in aerospace and electronic industries, Magnesium Alloys and their Applications (2000) 168-172.

[3] E. Zhang, D. Yin, L. Xu, L. Yang, K. Yang, Microstructure, mechanical and corrosion properties and biocompatibility of Mg–Zn–Mn alloys for biomedical application, Materials Science and Engineering: C 29(3) (2009) 987-993.

[4] U. Riaz, I. Shabib, W. Haider, The current trends of Mg alloys in biomedical applications—A review, Journal of Biomedical Materials Research Part B: Applied Biomaterials 107(6) (2019) 1970-1996.

[5] W. Yuan, S. Panigrahi, J.-Q. Su, R. Mishra, Influence of grain size and texture on Hall–Petch relationship for a magnesium alloy, Scripta Materialia 65(11) (2011) 994-997.

[6] H. Yu, Y. Xin, M. Wang, Q. Liu, Hall-Petch relationship in Mg alloys: a review, Journal of Materials Science & Technology 34(2) (2018) 248-256.

[7] N. Stanford, J. Geng, Y.B. Chun, C.H.J. Davies, J.F. Nie, M.R. Barnett, Effect of plate-shaped particle distributions on the deformation behaviour of magnesium alloy AZ91 in tension and compression, Acta materialia 60(1) (2012) 218-228.

[8] J.-F. Nie, Precipitation and hardening in magnesium alloys, Metallurgical and Materials Transactions A 43(11) (2012) 3891-3939.

[9] J.D. Robson, N. Stanford, M.R. Barnett, Effect of precipitate shape on slip and twinning in magnesium alloys, Acta materialia 59(5) (2011) 1945-1956.

[10] X. Ma, Q. Jiao, L.J. Kecskes, J.A. El-Awady, T.P. Weihs, Effect of basal precipitates on extension twinning and pyramidal slip: A micro-mechanical and electron microscopy study of a Mg–Al binary alloy, Acta Materialia 189 (2020) 35-46.

[11] A. Singh, M. Nakamura, M. Watanabe, A. Kato, A. Tsai, Quasicrystal strengthened Mg–Zn–Y alloys by extrusion, Scripta Materialia 49(5) (2003) 417-422.

[12] B. Wu, Y. Zhao, X. Du, Y. Zhang, F. Wagner, C. Esling, Ductility enhancement of extruded magnesium via yttrium addition, Materials Science and Engineering: A 527(16-17) (2010) 4334-4340.

[13] S. Sandlöbes, Z. Pei, M. Friák, L.-F. Zhu, F. Wang, S. Zaefferer, D. Raabe, J. Neugebauer, Ductility improvement of Mg alloys by solid solution: Ab initio modeling, synthesis and mechanical properties, Acta Materialia 70 (2014) 92-104.

[14] B. Guan, Y. Xin, X. Huang, P. Wu, Q. Liu, Quantitative prediction of texture effect on Hall–Petch slope for magnesium alloys, Acta Materialia 173 (2019) 142-152.

[15] Q. Yang, A. Ghosh, Deformation behavior of ultrafine-grain (UFG) AZ31B Mg alloy at room temperature, Acta materialia 54(19) (2006) 5159-5170.

[16] E. Hall, The deformation and ageing of mild steel: III discussion of results, Proceedings of the Physical Society. Section B 64(9) (1951) 747.

[17] R.W. Armstrong, 60 years of Hall-Petch: past to present nano-scale connections, Materials Transactions 55(1) (2014) 2-12.

[18] N. Petch, The cleavage strength of polycrystals, Journal of the Iron and Steel Institute 174 (1953) 25-28.

[19] R.W. Armstrong, Hall–Petch k dependencies in nanopolycrystals, Emerging Materials Research 3(6) (2014) 246-251.

[20] Y. Wang, H. Choo, Influence of texture on Hall–Petch relationships in an Mg alloy, Acta Materialia 81 (2014) 83-97.

[21] Y. Wang, C. Chang, C. Lee, H. Lin, J. Huang, Texture and weak grain size dependence in friction stir processed Mg–Al–Zn alloy, Scripta Materialia 55(7) (2006) 637-640.

[22] H. Yu, C. Li, Y. Xin, A. Chapuis, X. Huang, Q. Liu, The mechanism for the high dependence of the Hall-Petch slope for twinning/slip on texture in Mg alloys, Acta Materialia 128 (2017) 313-326.

[23] J. Liu, W. Xiong, A. Behera, S. Thompson, A.C. To, Mean-field polycrystal plasticity modeling with grain size and shape effects for laser additive manufactured FCC metals, International Journal of Solids and Structures 112 (2017) 35-42.

[24] S. Sun, V. Sundararaghavan, A probabilistic crystal plasticity model for modeling grain shape effects based on slip geometry, Acta Materialia 60(13-14) (2012) 5233-5244.

[25] G. Weng, A micromechanical theory of grain-size dependence in metal plasticity, Journal of the Mechanics and Physics of Solids 31(3) (1983) 193-203.

[26] B. Ravaji, S.P. Joshi, A crystal plasticity investigation of grain size-texture interaction in magnesium alloys, Acta Materialia 208 (2021) 116743.

[27] A. Singh, Y. Osawa, H. Somekawa, T. Mukai, Effect of microstructure on strength and ductility of high strength quasicrystal phase dispersed Mg–Zn–Y alloys, Materials Science and Engineering: A 611 (2014) 242-251.

[28] M.T. Andani, A. Lakshmanan, M. Karamooz-Ravari, V. Sundararaghavan, J. Allison, A. Misra, A quantitative study of stress fields ahead of a slip band blocked by a grain boundary in unalloyed magnesium, Scientific reports 10(1) (2020) 1-8.

[29] M.T. Andani, A. Lakshmanan, V. Sundararaghavan, J. Allison, A. Misra, Quantitative study of the effect of grain boundary parameters on the slip system level Hall-Petch slope for basal slip system in Mg-4Al, Acta Materialia 200 (2020) 148-161.

[30] A. Murphy-Leonard, The Effects Of Alloying And Grain Size On Fatigue Life Behavior, Cyclic Stress-Strain Behavior, and Microstructural Evolution of Unalloyed Mg and A Mg-Al Alloy, 2018.

[31] F. Bachmann, R. Hielscher, H. Schaeben, Texture analysis with MTEX–free and open source software toolbox, Solid State Phenomena, Trans Tech Publ, 2010, pp. 63-68.

[32] F. Bachmann, R. Hielscher, H. Schaeben, Grain detection from 2d and 3d EBSD data—Specification of the MTEX algorithm, Ultramicroscopy 111(12) (2011) 1720-1733.

[33] A.J. Wilkinson, G. Meaden, D.J. Dingley, High-resolution elastic strain measurement from electron backscatter diffraction patterns: new levels of sensitivity, Ultramicroscopy 106(4-5) (2006) 307-313.

[34] T. Britton, A.J. Wilkinson, High resolution electron backscatter diffraction measurements of elastic strain variations in the presence of larger lattice rotations, Ultramicroscopy 114 (2012) 82-95.

[35] M. Yaghoobi, S. Ganesan, S. Sundar, A. Lakshmanan, S. Rudraraju, J.E. Allison, V. Sundararaghavan, PRISMS-Plasticity: An open-source crystal plasticity finite element software, Computational Materials Science 169 (2019) 109078.

[36] B.A. Bilby, A.H. Cottrell, K. Swinden, The spread of plastic yield from a notch, Proceedings of the Royal Society of London. Series A. Mathematical and Physical Sciences 272(1350) (1963) 304-314.

[37] S. Taira, K. Tanaka, Y. Nakai, A model of crack-tip slip band blocked by grain boundary, Mechanics Research Communications 5(6) (1978) 375-381.

[38] S.T. Shiue, S. Lee, The effect of grain size on fracture: Dislocation-free zone in the front of the finite crack tip, Journal of applied physics 70(6) (1991) 2947-2953.

[39] N.I. Muskhelishvili, J.R.M. Radok, Singular integral equations: boundary problems of function theory and their application to mathematical physics, Courier Corporation2008.

[40] C. Zhao, X. Chen, J. Wang, T. Tu, Y. Dai, K.S. Shin, F. Pan, Strain Hardening Behavior in Mg–Al Alloys at Room Temperature, Advanced Engineering Materials 21(3) (2019) 1801062.

[41] E. Kröner, Allgemeine kontinuumstheorie der versetzungen und eigenspannungen, Archive for Rational Mechanics and Analysis 4(1) (1959) 273-334.

[42] E.H. Lee, Elastic-plastic deformation at finite strains, (1969).

[43] R.J. Asaro, A. Needleman, Overview no. 42 texture development and strain hardening in rate dependent polycrystals, Acta metallurgica 33(6) (1985) 923-953.

[44] L. Anand, Constitutive equations for hot-working of metals, International Journal of Plasticity 1(3) (1985) 213-231.

[45] S.R. Kalidindi, C.A. Bronkhorst, L. Anand, Crystallographic texture evolution in bulk deformation processing of FCC metals, Journal of the Mechanics and Physics of Solids 40(3) (1992) 537-569.

[46] M. Yaghoobi, K.S. Stopka, A. Lakshmanan, V. Sundararaghavan, J.E. Allison, D.L. McDowell, PRISMS-Fatigue computational framework for fatigue analysis in polycrystalline metals and alloys, npj Computational Materials 7(1) (2021) 1-12.

[47] Lakshmanan, A.; Yaghoobi, M.; Stopka, K.S.; Sundararaghavan, V. Crystal Plasticity Finite Element Modeling of Grain Size and Morphology Effects (Submitted).

[48] M.A. Groeber, M.A. Jackson, DREAM. 3D: a digital representation environment for the analysis of microstructure in 3D, Integrating materials and manufacturing innovation 3(1) (2014) 56-72.

[49] T. Long, C.S. Smith, Single-crystal elastic constants of magnesium and magnesium alloys, Acta Metallurgica 5(4) (1957) 200-207.

[50] L.J. Slutsky, C. Garland, Elastic constants of magnesium from 4.2 K to 300 K, Physical Review 107(4) (1957) 972.

[51] J. Zhang, S.P. Joshi, Phenomenological crystal plasticity modeling and detailed micromechanical investigations of pure magnesium, Journal of the Mechanics and Physics of Solids 60(5) (2012) 945-972.

[52] C. Geuzaine, J.F. Remacle, Gmsh: A 3-D finite element mesh generator with built-in pre-and post-processing facilities, International journal for numerical methods in engineering 79(11) (2009) 1309-1331.

[53] T.B. Britton, A.J. Wilkinson, Stress fields and geometrically necessary dislocation density distributions near the head of a blocked slip band, Acta Materialia 60(16) (2012) 5773-5782.

[54] T. Britton, A. Wilkinson, Measurement of residual elastic strain and lattice rotations with high resolution electron backscatter diffraction, Ultramicroscopy 111(8) (2011) 1395-1404.

[55] A. Jain, O. Duygulu, D. Brown, C. Tomé, S. Agnew, Grain size effects on the tensile properties and deformation mechanisms of a magnesium alloy, AZ31B, sheet, Materials Science and Engineering: A 486(1-2) (2008) 545-555.

[56] B. Raeisinia, S.R. Agnew, A. Akhtar, Incorporation of solid solution alloying effects into polycrystal modeling of Mg alloys, Metallurgical and Materials Transactions A 42(5) (2011) 1418-1430.

[57] K.G. Davis, Slip continuity across grain boundaries in aluminum, University of British Columbia, 1959.

[58] W. Bollmann, Crystal defects and crystalline interfaces, Springer Science & Business Media2012.

[59] L. Lim, R. Raj, The role of residual dislocation arrays in slip induced cavitation, migration and dynamic recrystallization at grain boundaries, Acta Metallurgica 33(12) (1985) 2205-2214.

[60] M. Marcinkowski, W.F. Tseng, Dislocation behavior at tilt boundaries of infinite extent, Metallurgical Transactions 1(12) (1970) 3397-3401.

[61] T. Lee, I. Robertson, H. Birnbaum, AnIn Situ transmission electron microscope deformation study of the slip transfer mechanisms in metals, Metallurgical Transactions A 21(9) (1990) 2437-2447.

[62] Z. Shen, R. Wagoner, W. Clark, Dislocation pile-up and grain boundary interactions in 304 stainless steel, Scripta metallurgica 20(6) (1986) 921-926.

[63] Z. Shen, R. Wagoner, W. Clark, Dislocation and grain boundary interactions in metals, Acta metall. 36(12) (1988) 3231-3242.

[64] T. Lee, I. Robertson, H. Birnbaum, TEM in situ deformation study of the interaction of lattice dislocations with grain boundaries in metals, Philosophical Magazine A 62(1) (1990) 131-153.

[65] A. Marano, L. Gélébart, S. Forest, Intragranular localization induced by softening crystal plasticity: Analysis of slip and kink bands localization modes from high resolution FFT-simulations results, Acta Materialia 175 (2019) 262-275.

[66] M. Zhang, F. Bridier, P. Villechaise, J. Mendez, D. McDowell, Simulation of slip band evolution in duplex Ti–6Al–4V, Acta materialia 58(3) (2010) 1087-1096.

[67] B. Ahmadikia, M.A. Kumar, I.J. Beyerlein, Effect of Neighboring Grain Orientation on Strain Localization in Slip Bands in HCP Materials, International Journal of Plasticity (2021) 103026.

[68] J. Luo, A. Ramazani, V. Sundararaghavan, Simulation of micro-scale shear bands using peridynamics with an adaptive dynamic relaxation method, International Journal of Solids and Structures 130 (2018) 36-48.

[69] A. Lakshmanan, J. Luo, I. Javaheri, V. Sundararaghavan, Three-dimensional crystal plasticity simulations using peridynamics theory and experimental comparison, International Journal of Plasticity 142 (2021) 102991.

[70] X. Gu, Q. Zhang, E. Madenci, Non-ordinary state-based peridynamic simulation of elastoplastic deformation and dynamic cracking of polycrystal, Engineering Fracture Mechanics 218 (2019) 106568.